High-Throughput Electrochemical Characterization of Aqueous Organic Redox Flow Battery Active Material

Eric M. Fell[†] and Michael J. Aziz[*,‡]

Harvard John A. Paulson School of Engineering and Applied Sciences, 29 Oxford Street, Cambridge, MA, 02138, USA

†*Electrochemical Society Student Member* ‡*Electrochemical Society Member*

* *Corresponding author*

E-mail: maziz@harvard.edu

Abstract

The development of redox-active organics for flow batteries providing long duration energy storage requires an accurate understanding of molecular lifetimes. Herein we report the development of a high-throughput setup for the cycling of redox flow batteries. Using common negolyte redox-active aqueous organics, we benchmark capacity fade rates and compare variations in measured cycling behavior of identical volumetrically unbalanced compositionally symmetric cells. We propose figures of merit for consideration when cycling sets of identical cells, and compare three common electrochemical cycling protocols typically used in battery cycling: constant current, constant current constant voltage, and constant voltage. Redox-active organics exhibiting either high or low capacity fade rates are employed in the cell cycling protocol comparison, with results shown from over 50 flow cells.

Introduction

Redox flow batteries (RFBs) are currently the only electrochemical energy storage technology capable of fully decoupled power and energy capacities. The incumbent electrolyte chemistry, the all-vanadium (VRFB), has the potential to experience significant deployment (estimated 100 GWh by 2030) but appears limited to the single-digit TWh scale by 2050, which is well below expected global energy storage needs.[1] Alternative redox-active chemistries are thus highly sought for next-generation RFBs, preferably as drop-in replacements for vanadium electrolytes. Redox-active organic molecules (RAOMs) constitute one such option, with essentially unlimited synthetic tunability allowing for the tailoring of redox potential, stability, solubility, and electrochemical kinetics.[2,3] Nevertheless, while RAOMs consisting of Earth-abundant elements are typically not limited by mining constraints (unlike vanadium or lithium), they have the deleterious tendency to degrade over time, adversely affecting battery performance.

One advantage of the VRFB electrolyte is the symmetric chemistry on which it is based, whereby the active species in both negolyte and posolyte share a single parent metal ion, differing only in oxidation state. Due to the nuclear stability of vanadium, capacity loss in VRFBs is dominated by crossover, which can be remedied by rebalancing techniques.[4,5] Thus, unlike RAOMs, the initial redox-active species can be used throughout the entirety of the VRFB lifetime.

In the case of RAOMs, judicious functionalization can be used to increase stability, but it typically adds significant chemical cost.[3,6,7] The use of potentially inexpensive RAOMs—instead of vanadium—to save on up-front capital costs incurs a financial penalty due to future replacement of degraded material, the trade-off of which can be compared by considering the time-value of money.[8] Capital cost and levelized cost of storage models for organic RFBs have been proposed to evaluate the techno-economics of RAOMs with finite electrolyte lifetimes and their necessary replacement,[9,10] as well as capacity recovery of degraded active species.[11] The consideration of capacity recovery of organics is critical, as decay

reversibility of various anthraquinone derivatives has recently been demonstrated via *in situ* chemical[12] and electrochemical[13] techniques. Notably, $/kWh outputs of these cost models are highly sensitive to the electrolyte cost and degradation rate—especially when considering the expected multi-decadal lifetime of installed grid energy storage systems. Our group has previously demonstrated that calendar life, rather than cycle life, limits molecular lifetimes in aqueous organic redox flow batteries (AORFBs) due to various molecular instabilities that lead to side reactions, thus inhibiting performance.[14] Understanding the uncertainty in measured lifetimes of promising RAOM candidates is therefore paramount at early stages of research, as capacity fade rates measured from short-term battery cycling experiments are often extrapolated years into the future and used to make go/no go decisions regarding further investigation of novel chemistries. As an instructive embellishment, an electrolyte demonstrating an immutable 0.01%/day capacity fade rate could still provide usable battery capacity after 20 years whereas, without replacement, an electrolyte demonstrating a 0.02%/day capacity fade rate could not. The ability to differentiate between such similarly low fade rates is a topic of this investigation.

Redox flow batteries can be operated via multiple electrochemical cycling protocols including constant current (CC), constant voltage (CV), constant current followed by constant voltage (CCCV), constant power, or combinations thereof. A commercial grid-scale flow battery may operate under any of these conditions, depending on its use case. Examples include highly variable charging/discharging for energy arbitrage (taking advantage of electricity prices that fluctuate throughout the day), load-leveling, firm capacity, or operating reserves and ancillary services. The temporal delineation of battery state of charge (SOC) is dictated by the current profile—itself often influenced by capacity loss mechanisms—resulting from an imposed electrochemical cycling protocol. Due to the multiple battery cycling protocols at the user's disposal, a distinction must be made regarding the purpose of a selected protocol when characterizing an AORFB. We define this distinction as a battery cycling test being carried out to characterize either the AORFB system performance as a whole, or the lifetime

and stability of the RAOM(s) of interest on a single side of the battery. An interpretation of this divide is the purpose of testing a full cell (consisting of a negolyte opposite a posolyte) versus a symmetric cell (same redox couple on both sides).

A full cell employs at least two separate redox couples with a non-zero voltage difference between their standard reduction potentials. Both negolyte and posolyte RAOMs may undergo decay mechanisms that differ in rate constants, and reaction orders, thus requiring separate characterization of the individual electrolytes (e.g., in a symmetric cell) and the manner in which they decay, before any meaningful understanding of full cell performance can be made. Extrapolation to an RFB system operating under various real-world cycling conditions requires, among other things, prior knowledge of capacity degradation rate as a function of SOC in each reservoir, in order to attribute the source of observed capacity fade to a specific electrolyte.

Our group has previously demonstrated that the use of potentiostatic holds on a volumetrically unbalanced compositionally symmetric cell is the most robust configuration to electrochemically characterize capacity fade rates resulting from molecular decomposition and/or apparent capacity fade mechanisms in individual RFB electrolytes.[14–16] As shown herein, when assessing electrolyte calendar stability, accurate characterization of capacity fade and the ability to fully access available capacity across all states of charge is limited to techniques that finish with a constant potential hold i.e., CCCV or CV. By varying battery cycling protocols, a wealth of information such as charge/discharge capacities, capacity fade rates, coulombic efficiency, duration of half-cycles, and cell overpotentials can be compared. In protocols that include sections of constant current, further analysis using differential capacity (dQ/dV), or capacity attained during CC vs CV sections of CCCV cycling, can also provide additional information on evolving cell status.

Experimental

Electrolyte preparation

Reagents used to prepare posolyte and negolyte solutions were purchased from Sigma-Aldrich and used with no further purification: potassium hydroxide, potassium ferrocyanide trihydrate. 2,6-dihydroxyanthraquinone (2,6-DHAQ) was purchased from Carbosynth (ID FD40589, >96% purity, 240.21 g/mol). (((9,10-dioxo-9,10-dihydroanthracene-2,6-diyl)bis-(oxy))bis(propane-3,1-diyl))bis(phosphonic acid) (2,6-DPPEAQ, ID D5765, >90% purity, 484.33 g/mol) and 4,4'-((9,10-anthraquinone-2,6-diyl)dioxy)dibutyrate (2,6-DBEAQ, ID D5764, >95% purity, 412.39 g/mol) were purchased from TCI America. Subsequently we refer to these chemicals as KOH, ferrocyanide, DHAQ, DBEAQ, and DPPEAQ, respectively. All electrolytes were prepared inside a N_2-filled glovebox (Vacuum Atmospheres Company) with <5 ppm of oxygen, using deoxygenated deionized water that had already equilibrated with the glovebox atmosphere over multiple months. Negolytes were prepared in 0.1 M concentrations of the redox-active species, with a final solution pH of 14. The set of cells for each experiment contained a respective anthraquinone negolyte chemistry at 50% SOC prepared in a single batch i.e., a large volume of negolyte was initially charged (reduced) in a single cell against a ferrocyanide posolyte at pH 14, and then mixed with an equal volume of the initial discharged (oxidized) negolyte to form a 50% SOC electrolyte. The electrolyte was then divided across all cells in a given set to make a 4.0 mL capacity limiting side (CLS) and a 6.0 mL non-capacity limiting side (NCLS) for each respective cell. Initiating a cell with identical 50% SOC electrolyte reservoirs, asymmetric in volumes, forms the basis of the volumetrically unbalanced compositionally symmetric cell method.[14]

Cell assembly

All volumetrically unbalanced compositionally symmetric flow cell cycling tests were carried out with cell hardware from Fuel Cell Technologies Inc. (Albuquerque, NM), assembled into

a zero-gap flow cell configuration, as described in a previous report.[17] Pyrosealed POCO graphite flow plates (9 in^2) with interdigitated flow patterns were used for both electrodes. Each electrode comprised a 5 cm^2 geometric surface area covered by a stack of two sheets of Sigracet GDL 39AA porous carbon paper (Fuel Cell Store) that had been pretreated by baking in air at 400°C for 24 h. The outer portion of the space between the electrodes was gasketed using Viton (PVDF) sheets (10 mils) with the area over the electrodes cut out. For all cell tests, a sheet of Nafion 117 (Ion Power Inc.) served as the ion-selective membrane between the carbon electrodes. All membranes were presoaked in 1 M KOH for two days to ion exchange the counter ions from protons to potassium ions. The torque applied during cell assembly was 60 lb-in (6.78 N·m) on each of eight 3/8"-24 bolts; thus the load applied per bolt was approximately 800 lbs. Electrolytes were fed into the cells through fluorinated ethylene propylene (FEP) tubing (each ∼10 inches long) at a rate of 60 mL/min, controlled by KNF diaphragm liquid pumps (FF 12 DCB-4). For 0.1 M electrolytes of the investigated redox species, and a typical maximum observed current (when cycled potentiostatically) of ∼60 mA/cm^2, flow factors[18] near 65 are expected at this flow rate. We have found that individual reservoirs mix best when the tubing inlet for cell ingress is placed near the bottom of a reservoir, while the tubing outlet for cell egress is placed just below the electrolyte meniscus. This configuration ensures that any change in electrolyte volume in the reservoir does not accidentally lead to the cell pumping dry.

High-throughput setup

Cells were cycled in the same glovebox that electrolytes were prepared in, which was equipped with battery lead binding posts and USB feedthroughs. Four-point connections were used between each cell and the battery cycler, therefore cell measurements were not affected by the added resistance of glovebox feedthroughs. A Novonix battery cycler equipped with a DC-offset unit supplying a voltage range of -1 to +4 V was used for all cell cycling. Glovebox temperature was recorded with an Arduino Uno Rev3 microcontroller equipped

with DHT22 temperature sensors, shown in **Fig. S1**. Cell temperature was measured with a K-type thermocouple (39095K96, McMaster-Carr) and recorded with a data acquisition module (TC-08, Omega). Diaphragm pumps were controlled individually by an Arduino-based system, and operated external to the glovebox via USB by way of a Python GUI. This setup allows for real-time management of electrolyte flow for controlled-atmosphere cells, *ex situ* from the glovebox. A single row of operating cells is shown in **Fig. 1**. Cells are modularized in individual containers containing a battery, two pumps, and two reservoirs (see **Fig. S2** for a single cell close-up).

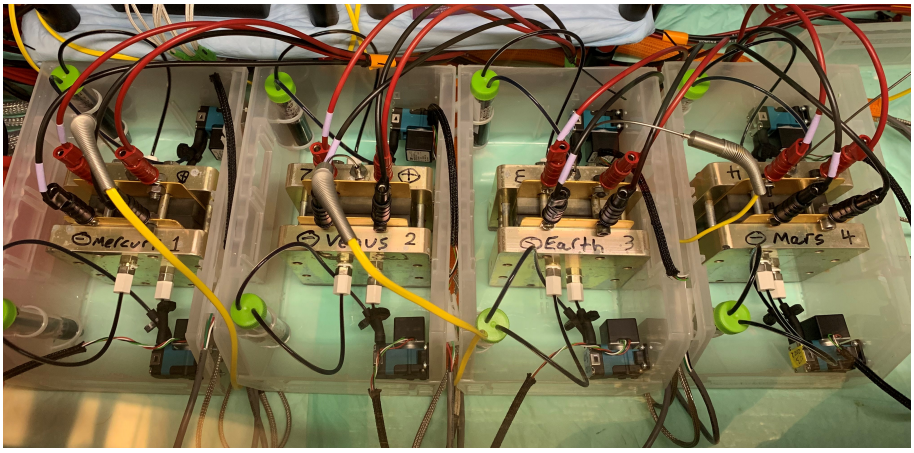

Figure 1: A row of modularized flow batteries in the high-throughput system.

Electrochemical cycling protocols

CLS and NCLS electrolytes were pumped through cells for roughly three hours before electrochemical cycling commenced. This ensured proper wetting and equilibration of cell components, as well as providing ample time for stabilization of the glovebox temperature which can fluctuate when cells are transferred in from the glovebox antechamber. The CLS of each cell is first reduced (charging), thus the first charge half-cycle capacity is roughly half of the total capacity (i.e., the CLS is reduced from 50% to 100% SOC) and the first oxidation (discharging) half-cycle capacity is ideally the total capacity (i.e., the CLS is oxidized from 100% to 0% SOC). Due to the expansion of the ordinate range that would be required, we

do not plot the first charging half-cycle, thus all coulombic efficiency figures herein start at the second full cycle i.e., second discharge capacity divided by second charge capacity. Voltage cutoffs were set to ±0.2 V for all CC cycling, and voltage holds were set to ±0.2 V (square wave in voltage with amplitude 0.2 V) with current cutoffs of 1 mA/cm^2 (geometric area) for CCCV and CV cycling. Electrochemical Impedance Spectroscopy (EIS) was performed before and after cell cycling with a Gamry Interface 1010B located inside the glovebox, with four-point cell connections. EIS was performed at open circuit voltage with a 10 mV amplitude AC potential at frequencies ranging from 20 kHz to 10 Hz. We report the high-frequency intercept of the real axis of a Nyquist plot as cell ohmic resistance. Pre-electrochemical-cycling EIS measurements were obtained with both CLS and NCLS at 50% SOC, whereas post-electrochemical-cycling EIS measurements were taken when the CLS was mostly discharged.

Results

High-throughput validation

A constant voltage cycling protocol was used to provide extreme yet realistic cell conditions by performing ∼100% depth of discharge (DoD) to access full capacity of the chemistry of interest. In **Fig. 2a** we plot the temporal capacity of a 0.1 M DPPEAQ pH 14 symmetric cell while measuring both glovebox and cell temperatures. Our lab experiences diurnal fluctuations in building temperature and the glovebox is not immune to these changes; they are only decreased in magnitude within the glovebox (typically less than 2°C swing). Cell temperature tracks with the glovebox temperature, as seen in **Fig. 2b**, and so for simplicity we use the continuously measured glovebox temperature as a proxy for all cell temperatures going forward. In the temporal capacity profile of the cell we observe a marked initial decrease in both charge and discharge capacities over the first half day of cycling, while **Fig. 2c** shows an increasing coulombic efficiency (CE) during this same period. This effect

should not be confused with that of residual dissolved oxygen, which would result in a similar marked drop in charge capacity and a distinct mirrored increase in discharge capacity over initial cycles, which also results in a low initial CE that increases over time (see e.g., low concentration symmetric cells in ref. 15).

The initial drop in capacity observed in **Fig. 2a** is often seen in AORFB cells with electrolytes that do not experience high capacity fade rates,[19,20] most likely because the drop is no longer hidden by fast degradation-induced capacity fade. Previous work that examined the impact of RAOM purification showed no effect on capacity fade rates, suggesting that the initial drop in measured capacity is unlikely to be due to impurities.[20] The initial increase in CE occurring simultaneously with the marked initial capacity drop also seems to support this conclusion. Irreversible capacity loss in the first few cycles has also been observed in various lithium-ion battery chemistries and is often attributed to parasitic electrochemical reactions occurring on the surface of the cathode materials and loss of active material due to irreversible structural changes,[21] slow intercalation kinetics,[22] or a combination of the two.[23] It is unclear how these effects could relate to AORFBs but one possible explanation could be that the initial capacity loss in AORFBs is somewhat capacitive in nature, as similar trends in capacity and CE have been observed in capacitive deionization cells employing carbon electrodes.[24] An investigation of the mechanism in AORFBs is outside of the scope of this work, but to obtain accurate capacity fade measurements we ensure that cell coulombic efficiency has stabilized before fitting temporal capacity data (typically after 1 day). An instantaneous capacity fade rate is calculated from the slope of the natural log of discharge half-cycle capacity vs time. We define the first figure of merit for the high-throughput system as the uncertainty in the measured instantaneous capacity fade rate of an individual cell. The margin of error of the regression slope at the 95% confidence level is reported herein as the ± uncertainty in a given fade rate. For the cell shown in **Fig. 2a**, we obtain an instantaneous capacity fade rate of 0.0567 ± 0.0008% per day. Typically, given a stable trend in temporal capacity fade, this single cell would now be deemed representative

of the investigated chemistry and capacity fade rate quantification would be considered complete. This is often the case in the AORFB community, and our group is no exception.[25–31] Small-batch synthesis, emblematic of academic exploration of novel RAOMs, encourages the practice of demonstrating a single cell for proof-of-concept. However, **Fig. 2a** represents only a single data point for the capacity fade rate of this electrolyte i.e., there is no indication of the statistical variation in measured fade rates at the given electrolyte and cell cycling conditions.

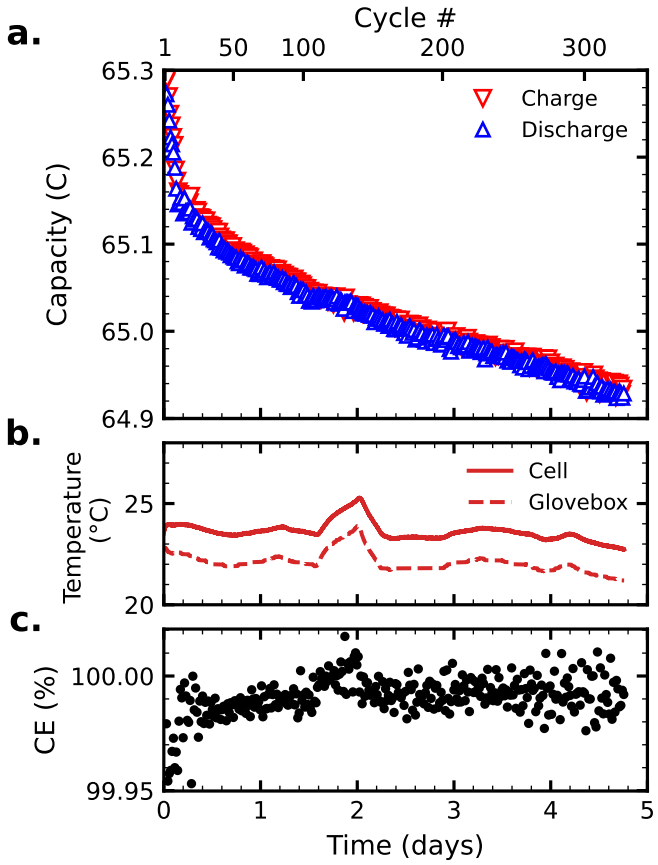

Figure 2: CV cycling of a 0.1 M DPPEAQ pH 14 symmetric cell (4.0 mL CLS vs 6.0 mL NCLS). (a) semi-log plot of temporal and cycle-based capacity; (b) cell and glovebox temperatures during cycling; and (c) coulombic efficiency.

The high-throughput setup allows for standard electrochemical cycling of RFBs under nominally identical conditions i.e., the same starting electrolyte, N_2 atmosphere, and temperature. Simultaneous testing of a set of identical cells with the same batch of electrolyte

removes the effects (if any) of batch-to-batch variations in concentration. Furthermore, the batch method establishes a uniform starting SOC for each cell (∼50%), and ensures that any fluctuations in O_2 ppm and glovebox temperature are experienced by all cells concurrently. Cell-to-cell variability was benchmarked in the high-throughput system by cycling eight identical 0.1 M DPPEAQ pH 14 symmetric cells potentiostatically, as seen in **Fig. 3**. All cells started with a 4.0 mL CLS and 6.0 mL NCLS, both initially at 50% SOC, with the same batch of electrolyte being dispersed in both reservoirs of each cell. Electrochemical cycling of all cells was initiated simultaneously. We plot temporal discharge capacity in **Fig. 3a** and note that each cell exhibits a slightly different initial capacity. The standard deviation in accessed capacity across cells is less than the uncertainty associated with error propagation from solution preparation and aliquoting (± 0.9 C). No trend in accessed capacity vs specific cell hardware used is observed in the present work when electrochemical cycling conditions are identical, see **Table S**1. Instantaneous capacity fade rates are calculated for each cell and reported in **Table S**2.

We define the second figure of merit for the high-throughput system as the average of instantaneous fade rates across a set of nominally identical cells, with standard deviation reported as the uncertainty. For the eight DPPEAQ cells of **Fig. 3**, this value is 0.07 ± 0.02 %/day. The significant standard deviation, relative to the average fade rate, masks the precision in individual cell fade rates e.g., cell#4 demonstrates an instantaneous fade rate of 0.0421 ± 0.0006 %/day. Therefore, coulometric precision is not an issue. In **Fig. 3b** the cycle-based capacity of the same cells is plotted, demonstrating a large cell-to-cell variation in total cycles performed during the five days of cell cycling. Although the duration of a potentiostatic half-cycle is dependent on the amount of degradation that has taken place (which is a time-dependent process), cells that cycle low capacity fade rate chemistries such as DPPEAQ will have potentiostatic cycle lengths predominantly dictated by cell ohmic resistance. The eight DPPEAQ cells demonstrate similar temporal capacity fade rates with time-denominated fade mechanisms, yet they perform a large range of total cycles over the

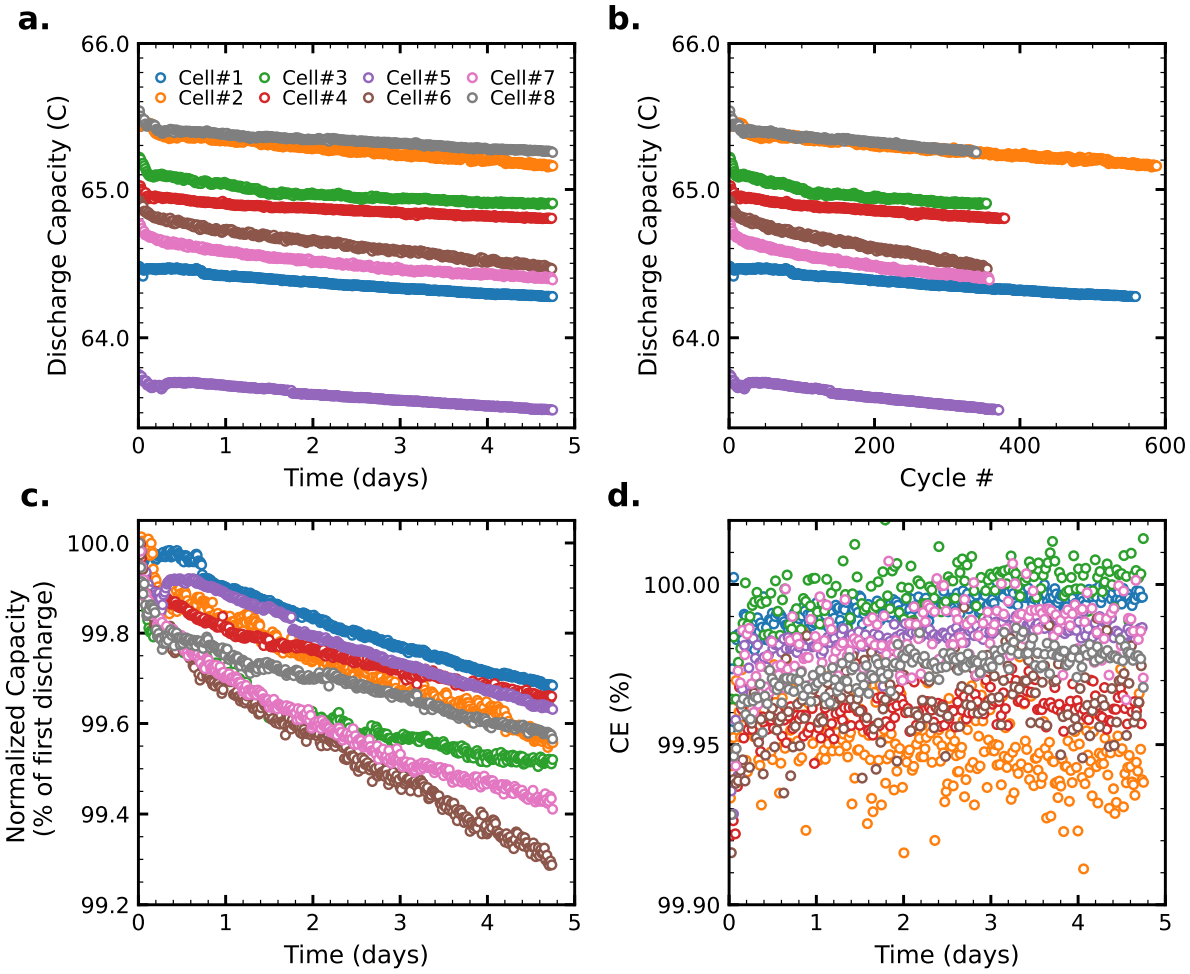

Figure 3: CV cycling of 0.1 M DPPEAQ pH 14 symmetric cells (4.0 mL CLS vs 6.0 mL NCLS). Semi-log plots of (a) temporal discharge capacity; (b) cycle-based discharge capacity; and (c) temporal discharge capacity normalized by the first discharge capacity. (d) Temporal coulombic efficiency, with every other cycle plotted for clarity.

same duration in **Fig. 3b**. This leads to ambiguous cycle-based capacity fade rates, thus demonstrating the futility in reporting only cycle-denominated metrics. Additionally, cells that differ in initial capacity cannot be compared meaningfully in % capacity fade per cycle unless the cycle period is identical between each cell. In **Fig. S3** we demonstrate how the length of CV discharge half-cycles of select DPPEAQ cells from **Fig. 3** is inversely correlated with temperature. We note that increased temperature decreases cycle duration, most likely due to increased membrane and electrolyte conductivity. However, the use of potentiostatic cycling protocols still ensures that no change in accessed capacity occurs due to fluctuations in glovebox temperature.

Given the subtle variation in initial accessed capacity of each cell, we plot the temporal dependence of the discharge capacity normalized by the first discharge half-cycle capacity of each cell in **Fig. 3c**. The ordinate spans less than 1% of capacity fade over the nearly five days of cell cycling but it is clear that there is a distribution, in terms of experimental variance in capacity data, across the eight cells. Finally in **Fig. 3d** we plot temporal coulombic efficiency of the eight cells. Again we see a range of average CE values across cells but observe no trend in instantaneous capacity fade rate vs average CE (seen in **Fig. S4a**), or cycle-based fade rate (seen in **Fig. S4b**). To our knowledge, this is the first literature report of cell performance variation in multiple identical AORFBs cycled simultaneously. Noise in the measured temporal capacity can often be attributed to the experimental setup of an AORFB. Capacity is reached via the diffusive mass transport of reactants to the electrodes; thus changes in reactant accessibility of the electrodes affect measured capacity. As previously noted in ref. 14, spontaneous changes in measured capacity can be caused by the formation of stagnant zones in electrolyte reservoirs, permeation of electrolyte to small recesses in tubing junctions, and splashing leading to droplets forming on the walls of the CLS reservoir. With judicious placement of tubing inlets/outlets, and the use of diaphragm pumps, we have greatly alleviated previous issues of splashing and droplet formation that had often contributed noise to our past work when cycling RFBs using peristaltic pumps.

With regards to crossover of RAOMs, the Schubert group has recently raised concerns that membrane crossover in AORFB symmetric cells could lead to misrepresented capacity fade trends.[20,32] However, this concern appears unwarranted given the multiple studies[28,31,33] of novel functionalized anthraquinone species or ferri-/ferrocyanide demonstrating permeabilities through as-received and ion-exchanged (sodium or potassium) Nafion on the order of 10^{-13} cm^2/s. Given the cell and reservoir configurations used in this study (4 mL CLS, 5 cm^2 area covered by Nafion 117 membrane), and assuming the unlikely case of species crossover solely from CLS to NCLS, a negolyte could only cross over at a rate equal to capacity loss of a fade rate of 6×10^{-5} %/day. Such low crossover rate is two orders of magnitude lower than the most stable AORFB capacity fade rate reported[25] to-date, thus capacity fade due to crossover in the symmetric cells reported in this work is negligible at best. It is expected that both size-based effects and charge-based exclusion of the alkaline anthraquinones studied in this work contribute to low permeability through the cation exchange membrane.[34] Studies that have reported significantly higher Nafion permeabilities for similar RAOMs subjected Nafion membranes to pretreatment (typically heating in deionized water, then soaking in dilute hydrogen peroxide).[17,35–46] While this treatment preferentially increases membrane conductivity,[47] it does so at the expense of increased membrane swelling which results in faster crossover, thus providing an excessively high permeability benchmark—handily beat when reporting novel membrane chemistries for AORFBs.

With the high-throughput setup, we can now vary multiple cycling parameters across multiple identical cells, performing many experiments in parallel. In this work we demonstrate the effect of electrochemical cycling protocols on negolyte chemistries exhibiting high or low stability, but this platform can also be used to investigate the parameter space of cell component materials interactions e.g., different membranes and/or electrodes in cells cycling the same RAOM chemistry, or exploration of electrolyte parameters such as concentration, pH, supporting electrolyte, etc. Additionally, we highlight unintended errors in cell cycling i.e., in **Fig. S5** we present trends in capacity curves when cell cycling goes awry, such as leaking

electrolytes. Symmetric cells that leak electrolyte from the CLS will typically demonstrate a relatively fast, linear capacity fade once a leak has commenced. Cells leaking from the NCLS will typically demonstrate a period of relatively stable capacity (fade) before "rolling over" and exhibiting fast(er) linear capacity fade. The region of rollover typically occurs when the NCLS has lost enough capacity to no longer be considered the NCLS. Temporal capacity trends in cells exhibiting rollover are often determined by a complex combination of capacity fade/leak rates as well as initial cell setup configurations such as volume ratio of CLS:NCLS. However, the distinction between slow capacity fade rates and slow leakage rates is often difficult to disentangle. For example, it can be challenging during post mortem failure analysis to determine if minor leakage has occurred within a cell i.e., leakage from active area into the inter-gasket region, because cell disassembly itself often causes small amounts of residual electrolyte displacement into the same region. Degradation rates of extremely stable chemistries often equate coulometrically to the amount of capacity present in single-digit microliters of electrolyte, assuming leakage is the sole cause of capacity fade.

Cycling protocol comparison

With the capability to run multiple identical cells, we first examined the effect of electrochemical cycling protocol on battery metrics such as capacity and capacity fade rates. Two AORFB negolytes, DHAQ and DBEAQ, were chosen for these experiments, with demonstrated capacity fade rates categorized[6] as either high or low, respectively. Although higher stability RAOMs have been reported, these chemistries were selected due to commercial availability. At pH 14 conditions, DHAQ-based cells have demonstrated high capacity fade of ∼5–8%/day, depending on concentration and voltage cutoffs,[12–14] while DBEAQ-based cells have demonstrated capacity fade of ∼0.008–0.040%/day depending on pH and concentration.[15] However, it has been previously noted that such low fade rates are often associated with a high relative experimental uncertainty, as the measured fade rates are highly sensitive to small changes in the leakage rates and crossover through the membrane.[6]

Constant current (CC)

We first cycled eight symmetric cells, each containing the same batch of 0.1 M DHAQ pH 14 electrolytes, as seen in **Fig. 4**. Each cell first performed ten cycles of regular CV cycling to access theoretical capacity, before switching to CC cycling. Four current densities were chosen for CC cycling, with two cell replicates each. Temporal discharge capacity is shown in **Fig. 4a**, and cycle-based discharge capacity in **Fig. 4b**. Again we note that the standard deviation in accessed capacity of the eight cells (see inset of **Fig. 4a**) is smaller than the uncertainty associated with solution preparation and aliquoting. Given the rapid capacity fade rate of this molecule, ∼0.9% total capacity loss occurs over the initial ten CV cycles. Three distinct trends are seen in the capacity data: 1) All cells instantly experience a drop in capacity upon switching to CC cycling, as previously demonstrated in ref. 14; 2) Cells with larger applied current densities demonstrate a larger drop in capacity upon switching to CC cycling, with varying amounts of capacity drop observed amongst cell replicates; 3) During CC cycling, cells with larger applied current densities demonstrate larger fluctuations in capacity. Most striking is the fact that changes in glovebox temperature (tracked throughout the experiment) correlate well with the temporal capacity fluctuations observed in all cells, most exacerbated in the two cells cycling at 20 mA/cm^2, as seen in **Fig. 4c**. What could explain this observation, and the reason for inter-cell-replicate variation in accessed capacity, is the effect of ohmic overpotential on cells with respect to voltage cutoffs during CC cycling. All cells have voltage cutoffs set to ±0.2 V but each pair of cell replicates experiences a different ohmic overpotential as a function of the applied current. We demonstrate this effect by plotting the percent of the tenth CV cycle discharge capacity that is accessed once cells switch to CC cycling, as a function of applied current, shown in **Fig. 4d**. Accessed capacity is seen to decrease as applied current increases, but the discrepancy in accessed capacity between cell replicates also increases with applied current. This variation is due to the fact that individual cells have slightly different ohmic resistances (typically less than 0.2 Ω deviation in this work) which, when applying higher currents, exacerbate differences in

ohmic overpotentials. By accounting for individual cell resistance (acquired from EIS) and the applied current, an ohmic iR drop can be approximated. A clear trend in the inability of cells to access full capacity at increased ohmic overpotentials is seen in **Fig. 4e**. Contributions to ohmic resistance are typically temperature-dependent, thus fluctuations in glovebox temperature will affect cell resistance, which dictates the amount of capacity accessed when using CC cycling protocols. Consequently, cells cycled galvanostatically with higher applied currents will be most susceptible to temperature variations. Diurnal shifts in glovebox temperature have also been shown to correlate with variations in accessed capacity via *ex situ* techniques such as amperometric state of health measurements in AORFB systems.[20]

An ohmic overpotential instantly restricts a cell by bringing the cell voltage closer to the voltage cutoffs (before even considering activation and concentration overpotentials). Thus the voltage window in which a cell is allowed to access capacity is significantly limited at larger cell resistance and/or higher applied current. As an example, an alkaline RFB cell employing a thick Nafion 117 membrane (potassium-exchanged) exhibiting an area specific resistance (ASR) of 5 $\Omega \cdot cm^2$ and cycling galvanostatically at 30 mA/cm^2, will automatically be penalized with a 0.15 V ohmic overpotential. With voltage cutoffs set to ± 0.2 V, only 50 mV remains in the voltage window budget, and the ability of the cell to access all available capacity before reaching voltage cutoffs is significantly hampered. While the example described here is for symmetric voltage cutoffs of a symmetric cell, the analogy still holds for a full cell (see e.g., the effect of increased membrane resistance on galvanostatically cycled cells in ref. 48 and ref. 49). This effect can be seen throughout the AORFB literature when galvanostatic charge/discharge voltage profiles are reported at multiple current densities. As current densities are increased in CC cycling, the accessed capacity of a given charge/discharge half-cycle tends to decrease. In the case of repeated charge/discharge cycling of an AORFB, this means that only a portion of the full SOC is accessed i.e., less than 100% DoD. Unless both the oxidized and reduced states of the RAOM are fully stable, purely galvanostatic cycling does not provide a true depiction of RAOM stability.

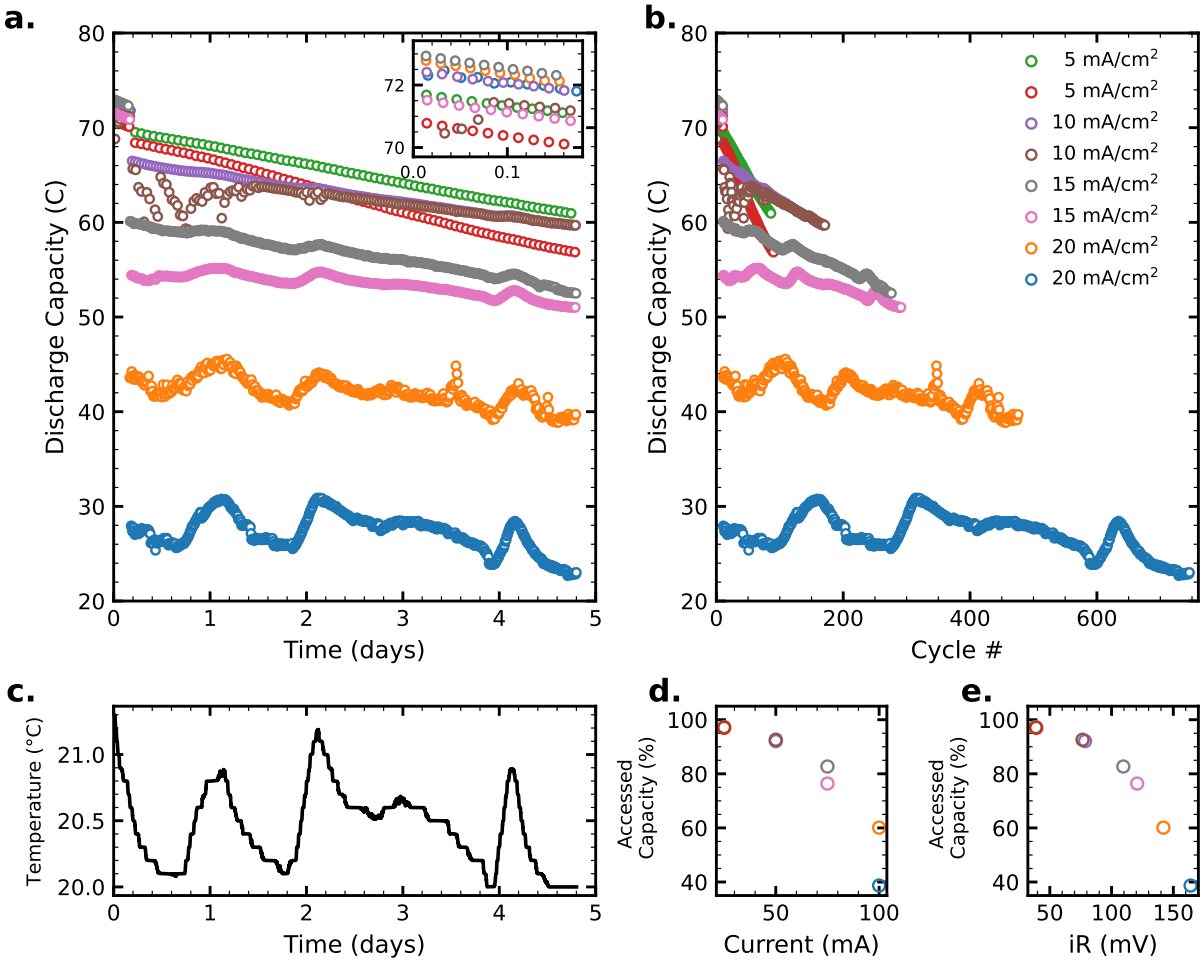

Figure 4: CC cycling of 0.1 M DHAQ pH 14 symmetric cells (4.0 mL CLS vs 6.0 mL NCLS). All cells began with 10 CV cycles (±0.2 V) to access full capacity, before switching to CC cycling. Plots of (a) temporal discharge capacity; (b) cycle-based discharge capacity; and (c) glovebox temperature over time. Percent of final CV discharge half-cycle capacity accessed when switching to CC cycling, as a function of (d) applied cell current; and (e) cell ohmic drop (applied current multiplied by cell resistance measured by EIS).

An identical constant current experiment was then performed with a more stable negolyte, DBEAQ, as seen in **Fig. 5**. Once again, a drop in capacity occurs upon switching from CV to CC cycling, with a larger drop resulting from higher applied currents as seen in **Fig. 5a&b**. Fluctuations in glovebox temperature, shown in **Fig. 5c**, correlate temporally with the capacity fluctuations of the cells, which intensify at higher applied currents. After correcting for individual cell resistance, accessed capacity (% of tenth CV cycle discharge capacity achieved upon switching to CC cycling) drops precipitously with increased ohmic overpotential, seen in **Fig. 5e**.

The results of **Fig. 4** and **Fig. 5** highlight an important, RAOM-stability-agnostic consideration: constant current (galvanostatic) cell cycling is essentially uncontrolled SOC-restriction when cell ASR is not constant for the duration of testing. Cell ohmic resistance (often dominated by membrane contribution) is always non-zero, thus any CC cycling instantly penalizes a cell with some amount of ohmic overpotential. If this overpotential is large enough to place the cell voltage close to a user-defined voltage cutoff, then, whether it be full or symmetric, a flow cell will not be able to achieve theoretical capacity using galvanostatic protocols. Examples in the literature that reversed the order of cycling operations shown here i.e., CC cycling for a number of cycles before switching to CV cycling, demonstrate an increase in accessed capacity upon switching to CV protocols.[14,50–52] Therefore, a capacity shortage is always present when CC cycling is employed, and it can often hide capacity degradation that continues to occur unabated. The question of whether the resulting inaccessible capacity matters or not, depends on the purpose of the cycling test being performed. For a commercial AORFB system composed of optimized cell stacks, CC cycling may be the required method for charge/discharge protocols, given the purpose of the energy storage device e.g., firm capacity vs energy arbitrage. However, if the purpose of testing is to quantify the SOC-dependent capacity fade rate of novel chemistries (the vast majority of academic pursuits in the organic RFB field), then cycling that provides ∼100% DoD to access full capacity is required, and CC cycling is simply unable to perform this task.

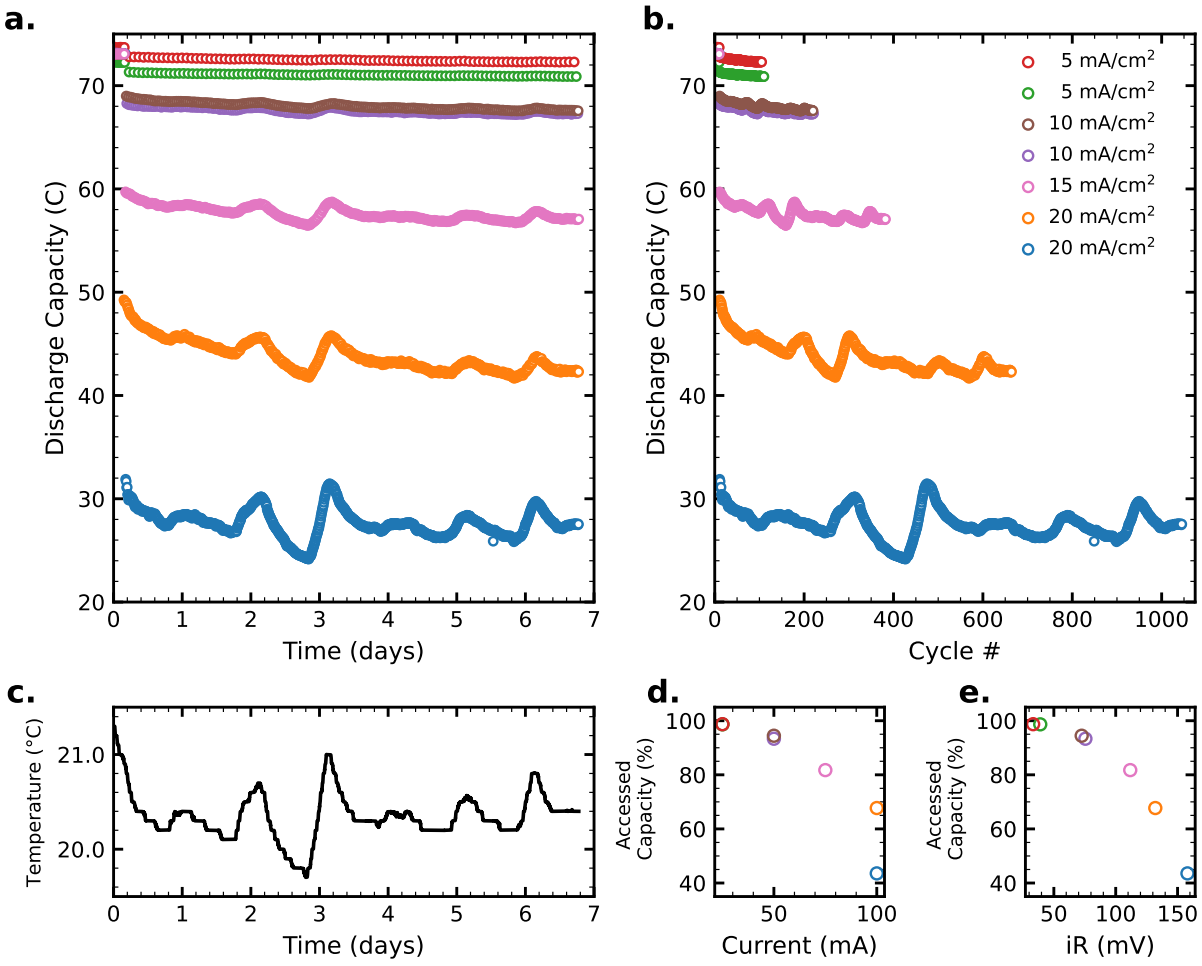

Figure 5: CC cycling of 0.1 M DBEAQ pH 14 symmetric cells (4.0 mL CLS vs 6.0 mL NCLS). All cells began with 10 CV cycles (±0.2 V) to access full capacity, before switching to CC cycling. Plots of (a) temporal discharge capacity; (b) cycle-based discharge capacity; and (c) glovebox temperature over time. Percent of final CV discharge half-cycle capacity accessed when switching to CC cycling, as a function of (d) applied cell current; and (e) cell ohmic drop (applied current multiplied by cell resistance measured by EIS).

Combined with high cell resistance and applied currents, data similar to the cells cycled galvanostatically at 20 mA/cm^2 in **Fig. 4** and **Fig. 5** are pervasive in the organic-based RFB literature. Temporal capacity plots with zoomed out ordinate axes, occasionally accompanied by unfounded claims of 0% capacity degradation, often demonstrate a significant discrepancy between theoretical and accessed capacity,[39,52–61] or even nonsensical increasing capacity over time,[46,48,62–69] when purely galvanostatic cycling is employed. Reporting only normalized capacity cycling data further obfuscates the capacity discrepancy caused by CC cycling. Oftentimes, diurnal temperature swings in a testing facility can be surmised from periodic fluctuations in temporal capacity or efficiency data of galvanostatically cycled cells seen in the literature.[33,40,41,44,49–51,61,63,66,69–71] Unfortunately, first accounts of novel RAOM chemistries are still being reported with only CC cycling provided as cell characterization. These studies often report the synthesis and cell-based characterization of a series of similar RAOMs derived from a family of molecules which, ideally, could provide valuable data for quantitative structure–property relationship studies.[63,66,68,70,72] Accurate measurements of RAOM stability are critical, not only to lifetime cost analysis of potential candidates for decadal RFB operation,[10] but also to the community-wide development of rich data sets of RAOM lifetimes. Such knowledge can complement high-throughput theoretical screening,[73–78] enhance machine learning capabilities,[79,80] and motivate RAOM stability prediction which still remains an open problem.

Given our CC cycling results from DHAQ and DBEAQ cells, it is not always apparent whether uncontrolled SOC-restriction i.e, galvanostatic cycling, will provide a lower or higher temporal capacity fade rate than when the full SOC is accessed. Thus, a measure of the intrinsic property of stability of many AORFB electrolytes previously reported is often wildly unreliable. This fact deserves increased emphasis in the literature; the measurement and reporting of a key parameter affecting the cost of a decadal AORFB system has yet to be conformed to a widely adopted standard. Though there may be value in cycling AORFBs with controlled SOC-restriction, whether it be to mitigate degradation caused by water split-

ting at extreme SOC[81] or investigate SOC-dependent degradation,[12] voltage holds should still be used, in combination with coulombic SOC-cutoffs. To characterize RAOM stability in these edge cases, it is important to periodically measure total capacity via 100% DoD cycles or via quantitative chemical analysis.

Constant current constant voltage (CCCV)

We next examined the effect of applying a voltage hold after galvanostatic cycling i.e, CCCV cycling protocols. Eight symmetric cells, each containing the same batch of 0.1 M DHAQ pH 14 electrolytes, performed ten cycles of regular CV cycling to access theoretical capacity before switching to CCCV cycling. Four current densities were chosen for the constant current portion of CCCV, two cell replicates each, with all cells finishing with voltage holds at ±0.2 V. Semi-log plots of temporal discharge capacity and cycle-based discharge capacity are shown in **Fig. 6a&b**, respectively. Although the full (remaining) capacity is accessed in each cell due to the potential hold of each half-cycle, the low current density cells perform roughly one third the number of cycles that the high current density cells achieve, for the same testing duration. Displayed as normalized capacity in **Fig. 6c**, cells exhibit a similar trend in capacity fade during the ten initial CV cycles but soon after begin to behave differently. DHAQ cells with the highest applied current density show the largest amount of capacity fade. Unlike the potentiostatically cycled DPPEAQ symmetric cells (**Fig. 3**), DHAQ CCCV cells appear to demonstrate a CC current density (and thus temporal capacity fade rate)-dependent coulombic efficiency with low current density cells demonstrating lower CE values, as seen in **Fig. 6d**. Temporal capacity fade rates are shown as a function of the applied current during CC sections of CCCV cycling, and as a function of individual cell ohmic iR drop (resistance acquired through EIS) in **Fig. 6e&f**, respectively. Cells with lower applied current densities during CC sections of CCCV cycling demonstrate lower temporal capacity fade rates. A similar comparison can be made when considering cycle-based fade rates as a function of the applied current during CC sections of CCCV cycling, and individual cell

ohmic iR drop in **Fig. 6g&h**, respectively. In this case, a clear trend is observed of decreasing cycle-based capacity fade rates with increased applied current densities i.e., cells that cycle more frequently. Additionally, there appears to be larger discrepancy amongst capacity fade rates of cell replicates as CC current densities decrease, even when differing cell resistance is accounted for, as seen in **Fig. 6f&h**.

To understand whether the observed effects of CC current density in CCCV cycling of DHAQ are applicable to other RAOMs, we repeated CCCV cycling experiments with symmetric cells containing identical 0.1 M DBEAQ pH 14 electrolytes, shown in **Fig. 7**. Temporal discharge capacity shown in **Fig. 7a** demonstrates an expected small relative variation in initial capacity accessed, due to standard deviation associated with uncertainty in the aliquoting process. In **Fig. 7b**, cells demonstrate an increased number of cycles with increased current density of the CC sections of CCCV cycling, with cell replicates showing slight variations due to differing cell ASR values. Plotting normalized temporal discharge capacity in **Fig. 7c** demonstrates the significant similarity in which these cells experience temporal capacity fade. The first cell (blue) operating at 20 mA/cm^2 experiences faster capacity fade and appears to be an outlier, possibly due to a very slow leak (unproven). Nevertheless, the increased stability of DBEAQ vs DHAQ at pH 14 is clearly demonstrated here, with all cells displaying less than 1% total capacity fade over approximately five days of cycling. Instantaneous capacity fade rates and associated uncertainties of the individual cells are reported in **Table S**2. The average temporal fade rate (second figure of merit for the high-throughput system, previously discussed) for the set of DBEAQ symmetric cells with CCCV cycling was 0.09 ± 0.02 %/day. No trend in capacity fade vs CE is discernible from the temporal CE values shown in **Fig. 7d**. Unlike in the DHAQ CCCV symmetric cells, we observe no trend in temporal capacity fade rates with respect to applied current densities of CC sections (**Fig. 7e**) or cell ohmic iR drop (**Fig. 7f**). We note that cells with noisy temporal discharge capacity data, e.g., the first cell replicate (pink) cycled at 15 mA/cm^2, also tend to demonstrate noisy temporal CE values whereas cells with less noisy

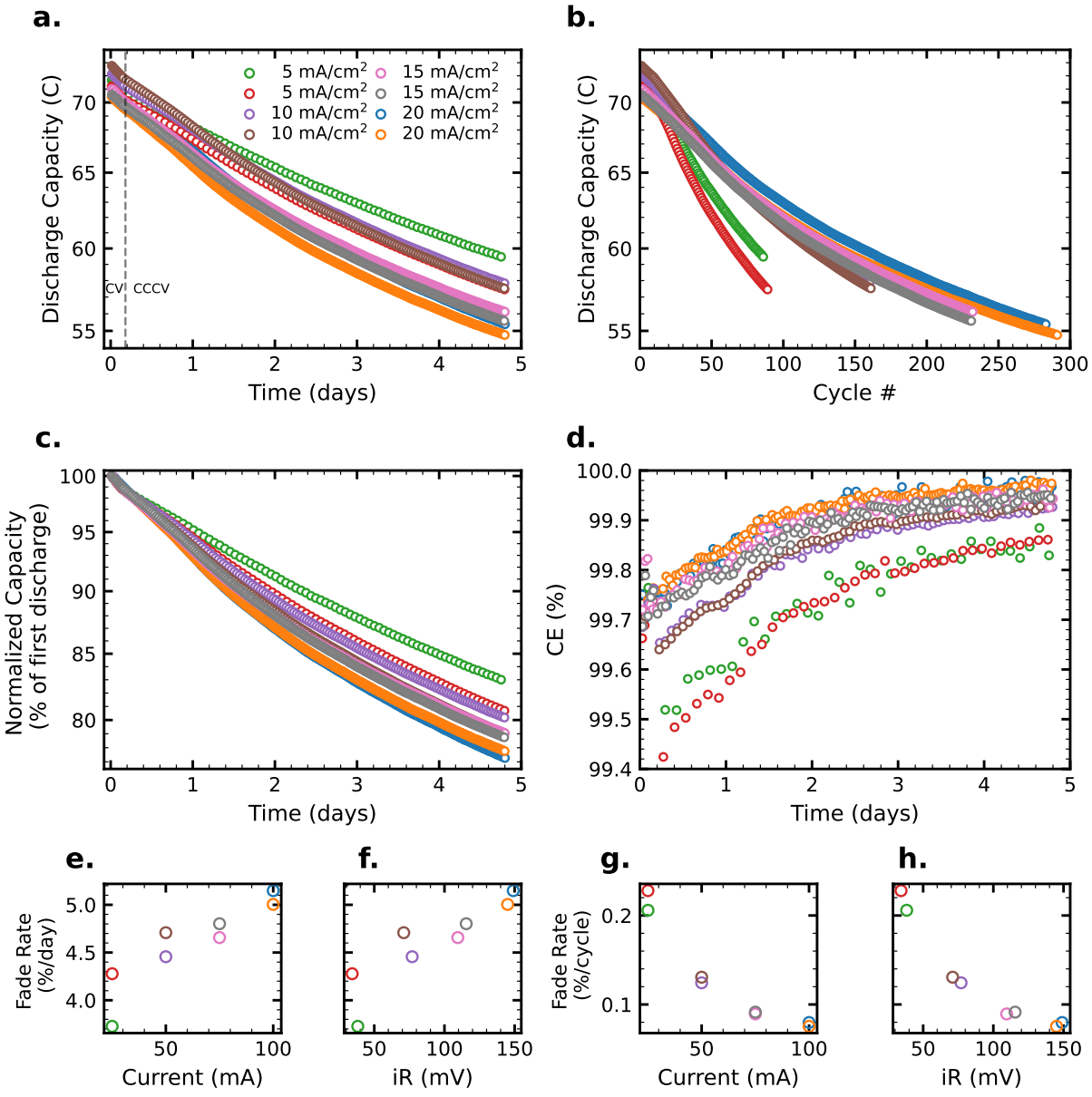

Figure 6: CCCV cycling of 0.1 M DHAQ pH 14 symmetric cells (4.0 mL CLS vs 6.0 mL NCLS). All cells began with 10 CV cycles (±0.2 V) to access full capacity, before switching to CCCV cycling. Semi-log plots of (a) temporal discharge capacity; (b) cycle-based discharge capacity; and (c) temporal discharge capacity normalized by the first discharge capacity. (d) Temporal coulombic efficiency, with every other cycle plotted for clarity. Instantaneous capacity fade rates during CCCV cycling as a function of (e) applied cell current; and (f) cell ohmic drop. Cycle-based capacity fade rates during CCCV cycling as a function of (g) applied cell current; and (h) cell ohmic drop.

capacity data, e.g., the second cell replicate (orange) cycled at 20 mA/cm^2, demonstrate less noisy CE. We assume that accessed capacity is also affected by how well the cell reservoirs maintain uniform mixing.

We compare temporal capacity fade rates against average CE during cycling, and cycle-based capacity fade rates, for both DHAQ and DBEAQ CCCV symmetric cells in **Fig. S6**. The set of DHAQ CCCV cells demonstrates a counter-intuitive trend of increasing average CE with increasing temporal capacity fade rate. These cells also show an inverse relationship between temporal and cycle-based capacity fade rates. Although the significance and interpretation of coulombic efficiency in AORFB symmetric cells is not well defined—and beyond the scope of this work—one possible hypothesis for the relationship between temporal and cycle-based capacity fade can be ascertained from the nature of the decomposition mechanism of DHAQ. Goulet & Tong *et al.*[12] previously showed that progressive loss of capacity in DHAQ-based alkaline AORFBs is primarily due to the formation of anthrone, via disproportionation of reduced (charged) DHAQ, followed by irreversible anthrone dimerization and further decomposition. However, both aeration[12] and electrochemical recomposition[13] techniques have been shown to rejuvenate decomposed DHAQ electrolytes. The loss of battery capacity can also be curtailed by avoiding high states of charge in DHAQ electrolytes through SOC-restriction techniques, or alternatively, by decreasing the amount of time spent at high SOC via judicious selection of electrochemical cycling protocols.

Recently, zero-dimensional modelling of AORFBs has shown that temporal capacity fade rates of RAOMs that demonstrate degradation mechanisms with reaction orders larger than one can differ depending on the applied current during the CC section of CCCV cycling, whereas RAOMs with first order decay mechanisms showed no current dependence on capacity fade rates in simulated CCCV cycling.[82] The reason for this effect is due to the distribution of the fraction of cycle time spent in a given SOC range. A higher applied current during CCCV cycling will lead to a cell hitting a voltage limit sooner (while still at more-intermediate-SOC) due to larger ohmic overpotentials, resulting in a longer duration

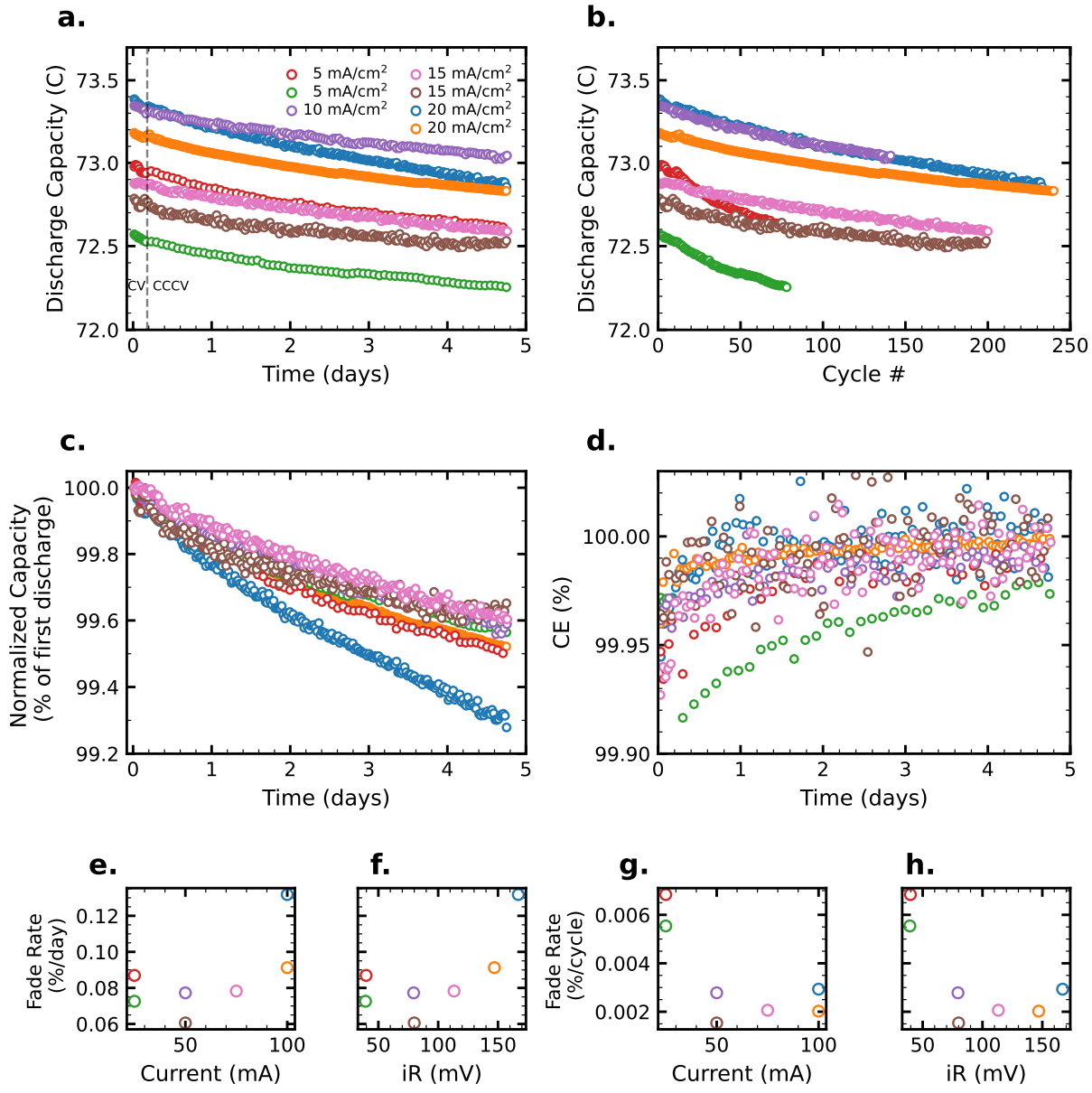

Figure 7: CCCV cycling of 0.1 M DBEAQ pH 14 symmetric cells (4.0 mL CLS vs 6.0 mL NCLS). All cells began with 10 CV cycles (±0.2 V) to access full capacity, before switching to CCCV cycling. Semi-log plots of (a) temporal discharge capacity; (b) cycle-based discharge capacity; and (c) temporal discharge capacity normalized by the first discharge capacity. (d) Temporal coulombic efficiency, with every other cycle plotted for clarity. Instantaneous capacity fade rates during CCCV cycling as a function of (e) applied cell current; and (f) cell ohmic drop. Cycle-based capacity fade rates during CCCV cycling as a function of (g) applied cell current; and (h) cell ohmic drop.

an electrolyte spends at extreme states of charge due to the CV hold with swiftly decaying current. Conversely, zero-dimensional modelling of CCCV cycling with lower applied currents resulted in a shorter relative duration that an electrolyte spends at extreme states of charge due to increased fraction of cycle time spent in the intermediate SOC range, enabled by a lower overpotential associated with the lower current (assuming identical cell ASR in both cases). Additionally, it was observed in ref. 82 that temporal capacity fade rates for simulated chemistries exhibiting first order capacity fade mechanisms remained invariant for CCCV and CV cycling protocols (employing the same voltage holds). Because the rate of reactant loss is SOC-dependent, and DHAQ decomposition is partially due to bimolecular disproportionation, cycling time spent at a given SOC may explain the observed effect of applied current during CCCV cycling on temporal capacity fade rate, as seen in **Fig. 6**. Similar AORFB results cycling the isomeric 2,3-DHAQ appear to agree with the observation of decreased applied current densities (during CC sections of CCCV cycling) leading to decreased temporal capacity fade rates and decreased CE values.[83] We hypothesize that current-density-dependent temporal capacity fade rates resulting from CCCV cycling may occur in other RAOMs that exhibit complex, coupled, degradation reactions such as the proposed mechanism in ref. 29. No current-dependent temporal capacity fade is observed for the DBEAQ symmetric cells of **Fig. 7**, as expected for an electrolyte that predominantly displays a first order decay mechanism.[15] Additionally, no relationship is seen between temporal capacity fade rates and average CE, or cycle-based fade rates, for DBEAQ CCCV cells as seen in **Fig. S6c&d**.

In **Fig. S7** we dissect the contribution of capacity accessed during CC and CV sections of the CCCV cycling of DHAQ symmetric cells shown in **Fig. 6**. Cells with low applied currents access the vast majority of available capacity during the CC sections. As applied currents increase during CCCV cycling, a greater fraction of overall capacity is accessed during the CV hold, due to the higher ohmic overpotential causing cells to hit voltage limits faster. Interestingly, accessed discharge capacity is greater than accessed charge capacity during CC

sections, at all applied currents in CCCV cycling of DHAQ symmetric cells. It is possible this effect is due to increased electrolyte conductivity of the charged negolyte (discharge half-cycles begin with fully charged electrolytes in CLS), or a difference in diffusion coefficients of reduced/oxidized species. Similar trends are observed for DBEAQ symmetric cells, with a dissection of capacity contributions during CCCV cycling shown in **Fig. S8**. Additionally, we can clearly see diurnal fluctuations in accessed charge and discharge capacities during the CC section of CCCV cycling in DBEAQ cells, increasingly exacerbated at higher applied currents, as was also demonstrated in **Fig. 4** & **Fig. 5**. This effect is somewhat hidden in the capacity dissection plots for DHAQ cells (**Fig. S7**) due to the significant capacity fade which is superimposed on the fluctuations. We show the overall glovebox temperature tracked throughout CCCV cycling experiments for DHAQ and DBEAQ cells in **Fig. S9**, and in both cases temperature swings correlate with capacity fluctuations during CC sections while CV sections are unaffected. This result should motivate the use of temperature-controlled cells whenever constant current cycling protocols are used i.e., CC and CCCV cycling. For a comparison to AORFB full cells, a similar dissection of capacity contributions during CCCV cycling is reported in ref. 84.

Electrochemical cycling protocols that include galvanostatic cycling allow for further examination of voltage profiles via differential capacity (dQ/dV) analysis. We provide a multi-cycle comparison of low/high applied current densities for CC and CCCV cycled symmetric cells, and the resulting dQ/dV analysis, for both DHAQ and DBEAQ cells in **Fig. S10** and **Fig. S11**, respectively. The cell voltage profiles of both chemistries demonstrate the effect of increased ohmic overpotential at increased applied current, illustrated by sharp drops in absolute voltage that occur at the start of each half-cycle. Although voltage profiles demonstrate the combined effect of ohmic, activation, and mass transport overpotentials superimposed on open circuit voltage, qualitative comparisons can be made in the region of the voltage profile directly after the ohmic drop i.e., the initial region of high curvature in the voltage profile that is dominated by activation overpotential. DHAQ is known to have a

larger difference in redox potentials of the two successive one-electron processes,[17] compared to that of DBEAQ,[15] and demonstrates a qualitatively larger contribution to activation overpotential in the cycling voltage profiles. From the dQ/dV analysis, the effect of rapid capacity fade can be seen prominently in the DHAQ cells, and the effect of increased applied current shifting the voltage at which the majority of capacity is accessed can be observed. If the NCLS volume were to be increased, with respect to the CLS volume, it could approximate the function of a reference electrode (assuming initial 50% SOC in the NCLS) and reported voltages could be replaced by potentials vs the utilized redox couple. We note that certain RAOMs may have potential-dependent capacity fade rates (such as viologens when accessing the reduced vs doubly reduced species[14,85]), and the potential which a molecule experiences in a cell is influenced by volumes and concentrations of the reservoirs, as well as the choice of full vs symmetric cells (see e.g., refs. 19 & 86).

Constant voltage (CV)

Culminating the comparison of electrochemical cycling protocols, we performed CV cycling of symmetric cells with either 0.1 M DHAQ or 0.1 M DBEAQ pH 14 electrolytes. All cells were cycled at ±0.2 V. Semi-log plots of temporal discharge capacity, cycle-based discharge capacity, and normalized temporal discharge capacity of DHAQ symmetric cells are shown in **Fig. 8a,b,c**, respectively. Given the nature of the complicated degradation mechanism of DHAQ discussed previously, we do not observe the linear (on a semi-log axis) temporal capacity fade one would expect for a first order decay mechanism. We acknowledge that reporting instantaneous capacity fade rates calculated from the log of capacity data implies first order degradation kinetics, which is not entirely valid for DHAQ at pH 14. However for the purpose of comparison with DBEAQ, we report instantaneous capacity fade rates of individual DHAQ cells in **Table S2** assuming a first order mechanism. The average temporal fade rate for the set of DHAQ symmetric cells with CV cycling was 4.6 ± 0.5 %/day. As a future line of work, modelling reaction decay kinetics of higher order degradation reactions

may provide insight on the observed trends in temporal capacity.

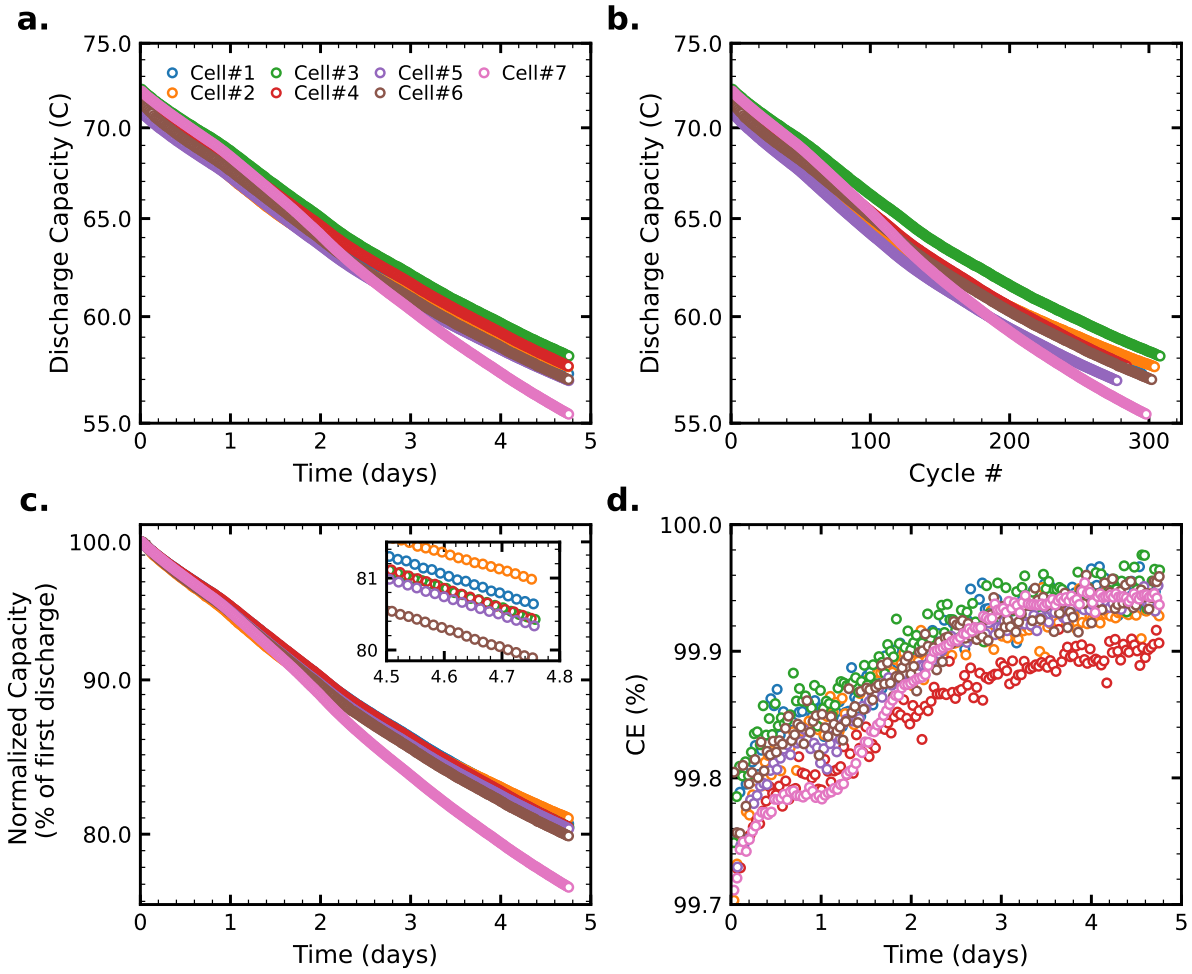

Figure 8: CV cycling of 0.1 M DHAQ pH 14 symmetric cells (4.0 mL CLS vs 6.0 mL NCLS). Semi-log plots of (a) temporal discharge capacity; (b) cycle-based discharge capacity; and (c) temporal discharge capacity normalized by the first discharge capacity. (d) Temporal coulombic efficiency, with every other cycle plotted for clarity.

We then performed an identical experiment with 0.1 M DBEAQ pH 14 symmetric cells cycled potentiostatically. Semi-log plots of temporal discharge capacity, cycle-based discharge capacity, and normalized temporal discharge capacity of DBEAQ symmetric cells are shown in **Fig. 9a,b,c**, respectively. Compared to the DHAQ cells with CV cycling, DBEAQ cells demonstrate a significant decrease in capacity fade, lower deviation in temporal capacity fade across cells, and higher CE values. The average temporal fade rate for the set of DBEAQ symmetric cells with CV cycling was 0.03 ± 0.01 %/day. For a comparison of CV cycling

metrics from the three chemistries shown in this work i.e., DPPEAQ, DHAQ, and DBEAQ, we refer the reader to **Fig. S4**. No correlation is observed between temporal capacity fade rates and average CE values for CV cells of all chemistries cycled. Additionally, in cycling protocols where potential holds were used to access maximum capacity, and no current-dependent temporal capacity fade was observed (CCCV cycling of DBEAQ, CV cycling of DBEAQ, DHAQ, DPPEAQ), we see no trend in a specific cell consistently displaying the highest/lowest temporal capacity fade rate. Thus it is improbable that cell hardware used in our study dictated the observed variation in temporal capacity fade rates. This clearly motivates simultaneous cycling of multiple replicate cells to avoid erroneously reporting a single (hapless) outlier as being representative of the capacity fade rate of a given chemistry. We summarize the statistical variation in temporal capacity fade rates of the aforementioned experiments (where no current-dependent degradation was observed) in **Fig. S12**.

One final consideration for potentiostatic cycling protocols is the effect of concentration on accessible capacity. Increased viscosity, decreased mass transfer coefficients, and poor reservoir mixing, often characteristic of concentrated AORFB electrolytes, can hinder the ability of lab-scale cells to access full capacity even when CV cycling protocols are used. This is not an issue for the low concentration RAOMs cycled in this study, but numerous literature examples have demonstrated an inability of cells to access more than 95% of theoretical capacity when cycling high concentration electrolytes potentiostatically.[3,25,29–31,50,87,88] We have previously seen that increased flow rates can provide increased accessed capacity, but academic lab-scale RFB systems are limited in this regard.[85] In these situations when no capacity fade is observed in concentrated electrolytes cycled potentiostatically but significant capacity is inaccessible, upper limits for temporal capacity fade rates should be reported as the difference in accessed vs. theoretical capacity, divided by duration of cycling. High-throughput systems are needed that can electrochemically cycle commercially relevant high concentration electrolytes with full capacity accessed, but the effective role of electrolyte energy density in AORFBs for stationary grid storage should also still be considered.[89,90]

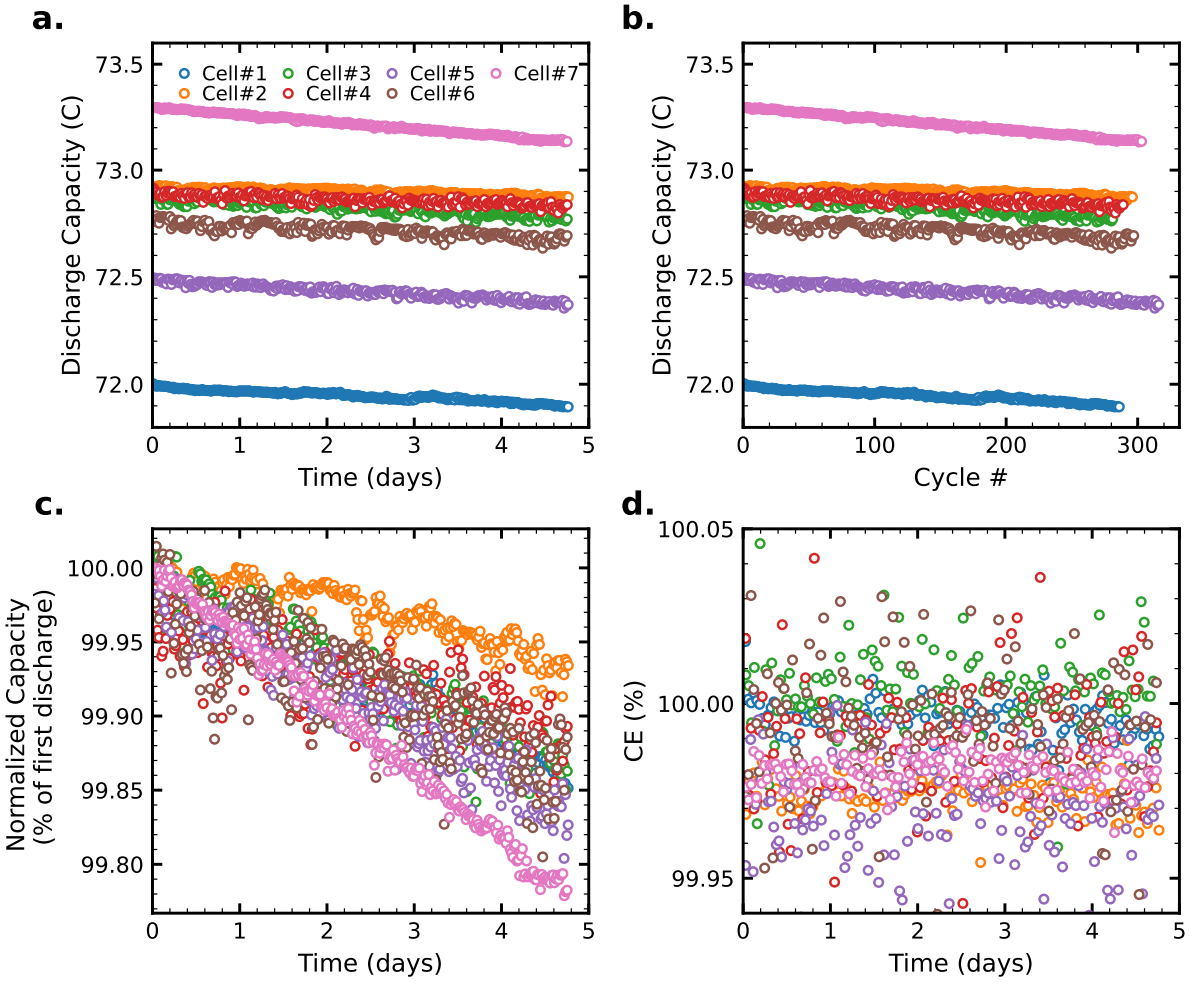

Figure 9: CV cycling of 0.1 M DBEAQ pH 14 symmetric cells (4.0 mL CLS vs 6.0 mL NCLS). Semi-log plots of (a) temporal discharge capacity; (b) cycle-based discharge capacity; and (c) temporal discharge capacity normalized by the first discharge capacity. (d) Temporal coulombic efficiency, with every other cycle plotted for clarity.

Conclusions

In this study we present results pertaining to the reproducibility of lifetime measurements for several aqueous organic redox flow battery electrolytes during electrochemical cycling in volumetrically unbalanced compositionally symmetric cells, in addition to results comparing multiple battery cycling protocols. Our general conclusions are summarized as follows:

1. High-throughput validation:

    a. Two figures of merit are proposed for reporting standardized temporal capacity fade rate measurements: the margin of error of the regression slope of the natural log of discharge capacity, at the 95% confidence level, representing the uncertainty in the measured instantaneous capacity fade rate of an individual cell; and in the case of testing multiple identical cells, the average of instantaneous fade rates across the set of replicates with standard deviation reported as the uncertainty.

    b. Simultaneous cycling of multiple AORFB volumetrically unbalanced compositionally symmetric cells under identical conditions with the same batch of electrolyte demonstrates cell-to-cell variability in temporal capacity fade rates. The standard deviation of the temporal capacity fade rates in individual sets is typically no more than 30% of the average. Furthermore, the absolute uncertainty in temporal capacity fade rates of individual cells appears to increase with fade rate.

    c. Cell-to-cell variation in measured temporal capacity fade rates must be reduced for rigorous demonstration of stable chemistries. When extrapolated to one year of cycling, the most stable set of cells reported herein (DBEAQ, CV cycling) exhibit a potentially unappealing standard deviation equivalent to a range in temporal capacity fade rates of approximately 7–15%/year.

2. Electrochemical cycling protocols:

a. Cell voltage during galvanostatic cycling is affected by fluctuations in ohmic overpotentials, via changes in cell resistance. Temperature fluctuations can drastically alter accessible capacity during cycling; this problem is exacerbated at high applied current densities and/or high cell ASR.

b. Total capacity accessed via cycling protocols that finish with a voltage hold (CCCV or CV) appears to be unaffected by temperature fluctuations. However, the length of time spent in a voltage hold is affected by temperature-dependent currents.

c. Comparing cycle-denominated capacity fade rates is meaningless if cells differ in initial capacity and cycle period length. The total number of demonstrated cycles in an AORFB is often reported as a figure of merit worthy of comparison, when in reality it is determined by the volume and concentration of electrolyte, temporal degradation rate, cell ASR, and current density, and thus is easily manipulated.

d. As predicted from zero-dimensional modelling, we hypothesize that RAOMs demonstrating decay mechanisms with reaction orders larger than one may display temporal capacity fade rates that are a function of applied current densities of the CC section of CCCV cycling protocols.

e. Regardless of the electrochemical cycling protocol used, AORFB testing should be complemented with real-time recording of cell temperature. Furthermore, temperature-controlled cells may lead to a reduction in noise of capacity data which will benefit high-precision measurement of RAOM lifetimes.

Acknowledgement

This research was supported by U.S. DOE award DE-AC05-76RL01830 through PNNL subcontract 535264. The authors thank Jim MacArthur of the Harvard Electronics Shop for assistance with pump controllers. We are very grateful for stimulating discussions and feed-

back from Prof. Marc-Antoni Goulet; Drs. Sharon Qian, Zhijiang Tang, Kiana Amini, and Yan Jing; and Jordan Sosa and Thomas George.

References

(1) Rodby, K. E.; Jaffe, R. L.; Olivetti, E. A.; Brushett, F. R. Materials availability and supply chain considerations for vanadium in grid-scale redox flow batteries. *Journal of Power Sources* **2023**, *560*, 232605.

(2) Winsberg, J.; Hagemann, T.; Janoschka, T.; Hager, M. D.; Schubert, U. S. Redox-Flow Batteries: From Metals to Organic Redox-Active Materials. *Angewandte Chemie International Edition* **2017**, *56*, 686–711.

(3) Jing, Y.; Fell, E. M.; Wu, M.; Jin, S.; Ji, Y.; Pollack, D. A.; Tang, Z.; Ding, D.; Bahari, M.; Goulet, M.-A.; Tsukamoto, T.; Gordon, R. G.; Aziz, M. J. Anthraquinone Flow Battery Reactants with Nonhydrolyzable Water-Solubilizing Chains Introduced via a Generic Cross-Coupling Method. *ACS Energy Letters* **2021**, 226–235.

(4) Skyllas-Kazacos, M.; Kazacos, M. State of charge monitoring methods for vanadium redox flow battery control. *Journal of Power Sources* **2011**, *196*, 8822–8827.

(5) Perry, M. L.; Saraidaridis, J. D.; Darling, R. M. Crossover mitigation strategies for redox-flow batteries. *Current Opinion in Electrochemistry* **2020**, *21*, 311–318.

(6) Kwabi, D. G.; Ji, Y.; Aziz, M. J. Electrolyte Lifetime in Aqueous Organic Redox Flow Batteries: A Critical Review. *Chemical Reviews* **2020**, *120*, 6467–6489.

(7) Gregory, T. D.; Perry, M. L.; Albertus, P. Cost and price projections of synthetic active materials for redox flow batteries. *Journal of Power Sources* **2021**, *499*, 229965.

(8) Yang, Z.; Tong, L.; Tabor, D. P.; Beh, E. S.; Goulet, M.-A.; De Porcellinis, D.; Aspuru-

Guzik, A.; Gordon, R. G.; Aziz, M. J. Alkaline Benzoquinone Aqueous Flow Battery for Large-Scale Storage of Electrical Energy. *Advanced Energy Materials* **2018**, *8*, 1702056.

(9) Dmello, R.; Milshtein, J. D.; Brushett, F. R.; Smith, K. C. Cost-driven materials selection criteria for redox flow battery electrolytes. *Journal of Power Sources* **2016**, *330*, 261–272.

(10) Brushett, F. R.; Aziz, M. J.; Rodby, K. E. On Lifetime and Cost of Redox-Active Organics for Aqueous Flow Batteries. *ACS Energy Letters* **2020**, *5*, 879–884.

(11) Rodby, K. E.; Perry, M. L.; Brushett, F. R. Assessing capacity loss remediation methods for asymmetric redox flow battery chemistries using levelized cost of storage. *Journal of Power Sources* **2021**, *506*, 230085.

(12) Goulet, M.-A.; Tong, L.; Pollack, D. A.; Tabor, D. P.; Odom, S. A.; Aspuru-Guzik, A.; Kwan, E. E.; Gordon, R. G.; Aziz, M. J. Extending the Lifetime of Organic Flow Batteries via Redox State Management. *Journal of the American Chemical Society* **2019**, *141*, 8014–8019.

(13) Jing, Y.; Zhao, E. W.; Goulet, M.-A.; Bahari, M.; Fell, E. M.; Jin, S.; Davoodi, A.; Jónsson, E.; Wu, M.; Grey, C. P.; Gordon, R. G.; Aziz, M. J. In situ electrochemical recomposition of decomposed redox-active species in aqueous organic flow batteries. *Nature Chemistry* **2022**, *14*, 1103–1109.

(14) Goulet, M.-A.; Aziz, M. J. Flow Battery Molecular Reactant Stability Determined by Symmetric Cell Cycling Methods. *Journal of The Electrochemical Society* **2018**, *165*, A1466–A1477.

(15) Kwabi, D. G.; Lin, K.; Ji, Y.; Kerr, E. F.; Goulet, M.-A.; De Porcellinis, D.; Tabor, D. P.; Pollack, D. A.; Aspuru-Guzik, A.; Gordon, R. G.; Aziz, M. J. Alkaline Quinone Flow Battery with Long Lifetime at pH 12. *Joule* **2018**, *2*, 1894–1906.

(16) Fell, E. M.; De Porcellinis, D.; Jing, Y.; Gutierrez-Venegas, V.; Gordon, R. G.; Granados-Focil, S.; Aziz, M. J. Long-term stability of ferri-/ferrocyanide as an electroactive component for redox flow battery applications: On the origin of apparent capacity fade. *ChemRxiv* **2022**,

(17) Lin, K.; Chen, Q.; Gerhardt, M. R.; Tong, L.; Kim, S. B.; Eisenach, L.; Valle, A. W.; Hardee, D.; Gordon, R. G.; Aziz, M. J.; Marshak, M. P. Alkaline quinone flow battery. *Science* **2015**, *349*, 1529–1532.

(18) Li, Y.; Skyllas-Kazacos, M.; Bao, J. A dynamic plug flow reactor model for a vanadium redox flow battery cell. *Journal of Power Sources* **2016**, *311*, 57–67.

(19) Amini, K.; Fell, E. M.; Aziz, M. J. The Poor Academic's DC-Offset for Reversing Polarity in Electrochemical Cells: Application to Redox Flow Cells. *Journal of The Electrochemical Society* **2022**, *169*, 090527.

(20) Volodin, I. A.; Stolze, C.; Nolte, O.; Rohland, P.; Hager, M. D.; Schubert, U. S. State and Prospects of Unbalanced, Compositionally Symmetric Flow Battery Cycling and Steady-State Amperometry Techniques for Electrolyte Stability Assessment: The Case of Methyl Viologen. *ACS Applied Energy Materials* **2023**, *6*, 302–316.

(21) Choi, J.; Manthiram, A. Investigation of the Irreversible Capacity Loss in the Layered $LiNi_{1/3}$ $Mn_{1/3}Co_{1/3}O_2$ Cathodes. *Electrochemical and Solid-State Letters* **2005**, *8*, C102.

(22) Kasnatscheew, J.; Evertz, M.; Streipert, B.; Wagner, R.; Klöpsch, R.; Vortmann, B.; Hahn, H.; Nowak, S.; Amereller, M.; Gentschev, A.-C.; Lamp, P.; Winter, M. The truth about the 1st cycle Coulombic efficiency of $LiNi_{1/3}Co_{1/3}Mn_{1/3}O_2$ (NCM) cathodes. *Physical Chemistry Chemical Physics* **2016**, *18*, 3956–3965.

(23) Zhou, H.; Xin, F.; Pei, B.; Whittingham, M. S. What Limits the Capacity of Layered Oxide Cathodes in Lithium Batteries? *ACS Energy Letters* **2019**, *4*, 1902–1906.

(24) Uwayid, R.; Seraphim, N. M.; Guyes, E. N.; Eisenberg, D.; Suss, M. E. Characterizing and mitigating the degradation of oxidized cathodes during capacitive deionization cycling. *Carbon* **2021**, *173*, 1105–1114.

(25) Wu, M.; Jing, Y.; Wong, A. A.; Fell, E. M.; Jin, S.; Tang, Z.; Gordon, R. G.; Aziz, M. J. Extremely Stable Anthraquinone Negolytes Synthesized from Common Precursors. *Chem* **2020**, *6*, 1432–1442.

(26) Li, Y.; Xu, Z.; Liu, Y.; Jin, S.; Fell, E. M.; Wang, B.; Gordon, R. G.; Aziz, M. J.; Yang, Z.; Xu, T. Functioning Water-Insoluble Ferrocenes for Aqueous Organic Flow Battery via Host–Guest Inclusion. *ChemSusChem* **2021**, *14*, 745–752.

(27) Wu, M.; Bahari, M.; Fell, E. M.; Gordon, R. G.; Aziz, M. J. High-performance anthraquinone with potentially low cost for aqueous redox flow batteries. *Journal of Materials Chemistry A* **2021**, *9*, 26709–26716.

(28) Wu, M.; Bahari, M.; Jing, Y.; Amini, K.; Fell, E. M.; George, T. Y.; Gordon, R. G.; Aziz, M. J. Highly Stable, Low Redox Potential Quinone for Aqueous Flow Batteries. *Batteries & Supercaps* **2022**, *5*, e202200009.

(29) Gao, J.; Amini, K.; George, T. Y.; Jing, Y.; Tsukamoto, T.; Xi, D.; Gordon, R. G.; Aziz, M. J. A High Potential, Low Capacity Fade Rate Iron Complex Posolyte for Aqueous Organic Flow Batteries. *Advanced Energy Materials* **2022**, *12*, 2202444.

(30) Kerr, E. F.; Tang, Z.; George, T. Y.; Jin, S.; Fell, E. M.; Amini, K.; Jing, Y.; Wu, M.; Gordon, R. G.; Aziz, M. J. High Energy Density Aqueous Flow Battery Utilizing Extremely Stable, Branching-Induced High-Solubility Anthraquinone near Neutral pH. *ACS Energy Letters* **2023**, *8*, 600–607.

(31) Amini, K.; Kerr, E. F.; George, T. Y.; Alfaraidi, A. M.; Jing, Y.; Tsukamoto, T.; Gordon, R. G.; Aziz, M. J. An Extremely Stable, Highly Soluble Monosubstituted An-

thraquinone for Aqueous Redox Flow Batteries. *Advanced Functional Materials* **2023**, *33*, 2211338.

(32) Nolte, O.; Volodin, I. A.; Stolze, C.; Hager, M. D.; Schubert, U. S. Trust is good, control is better: a review on monitoring and characterization techniques for flow battery electrolytes. *Materials Horizons* **2021**, *8*, 1866–1925.

(33) Robb, B. H.; George, T. Y.; Davis, C. M.; Tang, Z.; Fujimoto, C. H.; Aziz, M. J.; Marshak, M. P. Sulfonated Diels-Alder Poly(phenylene) Membrane for Efficient Ion-Selective Transport in Aqueous Metalorganic and Organic Redox Flow Batteries. *Journal of The Electrochemical Society* **2023**, *170*, 030515.

(34) George, T. Y.; Kerr, E. F.; Haya, N. O.; Alfaraidi, A. M.; Gordon, R. G.; Aziz, M. J. Size and Charge Effects on Crossover of Flow Battery Reactants Evaluated by Quinone Permeabilities Through Nafion. *Journal of The Electrochemical Society* **2023**, *170*, 040509.

(35) De Porcellinis, D.; Mecheri, B.; D'Epifanio, A.; Licoccia, S.; Granados-Focil, S.; Aziz, M. J. Communication—Sulfonated Poly (ether ether ketone) as Cation Exchange Membrane for Alkaline Redox Flow Batteries. *Journal of The Electrochemical Society* **2018**, *165*, A1137.

(36) Baran, M. J.; Braten, M. N.; Sahu, S.; Baskin, A.; Meckler, S. M.; Li, L.; Maserati, L.; Carrington, M. E.; Chiang, Y.-M.; Prendergast, D.; Helms, B. A. Design Rules for Membranes from Polymers of Intrinsic Microporosity for Crossover-free Aqueous Electrochemical Devices. *Joule* **2019**, *3*, 2968–2985.

(37) Tan, R.; Wang, A.; Malpass-Evans, R.; Williams, R.; Zhao, E. W.; Liu, T.; Ye, C.; Zhou, X.; Darwich, B. P.; Fan, Z.; Turcani, L.; Jackson, E.; Chen, L.; Chong, S. Y.; Li, T.; Jelfs, K. E.; Cooper, A. I.; Brandon, N. P.; Grey, C. P.; McKeown, N. B.;

Song, Q. Hydrophilic microporous membranes for selective ion separation and flow-battery energy storage. *Nature Materials* **2020**, *19*, 195–202.

(38) Zhao, E. W.; Liu, T.; Jónsson, E.; Lee, J.; Temprano, I.; Jethwa, R. B.; Wang, A.; Smith, H.; Carretero-González, J.; Song, Q.; Grey, C. P. In situ NMR metrology reveals reaction mechanisms in redox flow batteries. *Nature* **2020**, *579*, 224–228.

(39) Zuo, P.; Li, Y.; Wang, A.; Tan, R.; Liu, Y.; Liang, X.; Sheng, F.; Tang, G.; Ge, L.; Wu, L.; Song, Q.; McKeown, N. B.; Yang, Z.; Xu, T. Sulfonated Microporous Polymer Membranes with Fast and Selective Ion Transport for Electrochemical Energy Conversion and Storage. *Angewandte Chemie International Edition* **2020**, *59*, 9564–9573.

(40) Ye, C.; Wang, A.; Breakwell, C.; Tan, R.; Grazia Bezzu, C.; Hunter-Sellars, E.; Williams, D. R.; Brandon, N. P.; Klusener, P. A. A.; Kucernak, A. R.; Jelfs, K. E.; McKeown, N. B.; Song, Q. Development of efficient aqueous organic redox flow batteries using ion-sieving sulfonated polymer membranes. *Nature Communications* **2022**, *13*, 3184.

(41) Ye, C.; Tan, R.; Wang, A.; Chen, J.; Comesaña Gándara, B.; Breakwell, C.; Alvarez-Fernandez, A.; Fan, Z.; Weng, J.; Bezzu, C. G.; Guldin, S.; Brandon, N. P.; Kucernak, A. R.; Jelfs, K. E.; McKeown, N. B.; Song, Q. Long-Life Aqueous Organic Redox Flow Batteries Enabled by Amidoxime-Functionalized Ion-Selective Polymer Membranes. *Angewandte Chemie* **2022**, *134*, e202207580.

(42) Wang, A.; Tan, R.; Liu, D.; Lu, J.; Wei, X.; Alvarez-Fernandez, A.; Ye, C.; Breakwell, C.; Guldin, S.; Kucernak, A. R.; Jelfs, K. E.; Brandon, N. P.; McKeown, N. B.; Song, Q. Ion-Selective Microporous Polymer Membranes with Hydrogen-Bond and Salt-Bridge Networks for Aqueous Organic Redox Flow Batteries. *Advanced Materials* **2023**, *35*, 2210098.

(43) Wu, B.; Aspers, R. L. E. G.; Kentgens, A. P. M.; Zhao, E. W. Operando benchtop

NMR reveals reaction intermediates and crossover in redox flow batteries. *Journal of Magnetic Resonance* **2023**, *351*, 107448.

(44) Zuo, P.; Ye, C.; Jiao, Z.; Luo, J.; Fang, J.; Schubert, U. S.; McKeown, N. B.; Liu, T. L.; Yang, Z.; Xu, T. Near-frictionless ion transport within triazine framework membranes. *Nature* **2023**, *617*, 299–305.

(45) Latchem, E. J.; Kress, T.; Klusener, P. A. A.; Vasant Kumar, R.; Forse, A. C. Charge-dependent crossover in aqueous organic redox flow batteries revealed using on-line NMR spectroscopy. *ChemRxiv* **2023**,

(46) Tan, R.; Wang, A.; Ye, C.; Li, J.; Liu, D.; Darwich, B. P.; Petit, L.; Fan, Z.; Wong, T.; Alvarez-Fernandez, A.; Furedi, M.; Guldin, S.; Breakwell, C. E.; Klusener, P. A. A.; Kucernak, A. R.; Jelfs, K. E.; McKeown, N. B.; Song, Q. Thin Film Composite Membranes with Regulated Crossover and Water Migration for Long-Life Aqueous Redox Flow Batteries. *Advanced Science* **2023**, *n/a*, 2206888.

(47) Kusoglu, A.; Weber, A. Z. New Insights into Perfluorinated Sulfonic-Acid Ionomers. *Chemical Reviews* **2017**, *117*, 987–1104.

(48) Robb, B. H.; Waters, S. E.; Saraidaridis, J. D.; Marshak, M. P. Realized potential as neutral pH flow batteries achieve high power densities. *Cell Reports Physical Science* **2022**, *3*, 101118.

(49) Tsehaye, M. T.; Yang, X.; Janoschka, T.; Hager, M. D.; Schubert, U. S.; Planes, E.; Alloin, F.; Iojoiu, C. Anion exchange membranes with high power density and energy efficiency for aqueous organic redox flow batteries. *Electrochimica Acta* **2023**, *438*, 141565.

(50) Pang, S.; Wang, X.; Wang, P.; Ji, Y. Biomimetic Amino Acid Functionalized Phenazine Flow Batteries with Long Lifetime at Near-Neutral pH. *Angewandte Chemie International Edition* **2021**, *60*, 5289–5298.

(51) Xu, J.; Pang, S.; Wang, X.; Wang, P.; Ji, Y. Ultrastable aqueous phenazine flow batteries with high capacity operated at elevated temperatures. *Joule* **2021**, *5*, 2437–2449.

(52) Li, L.; Su, Y.; Ji, Y.; Wang, P. A Long-Lived Water-Soluble Phenazine Radical Cation. *Journal of the American Chemical Society* **2023**, *145*, 5778–5785.

(53) Liu, T.; Wei, X.; Nie, Z.; Sprenkle, V.; Wang, W. A Total Organic Aqueous Redox Flow Battery Employing a Low Cost and Sustainable Methyl Viologen Anolyte and 4-HO-TEMPO Catholyte. *Advanced Energy Materials* **2016**, *6*, 1501449.

(54) Orita, A.; Verde, M. G.; Sakai, M.; Meng, Y. S. A biomimetic redox flow battery based on flavin mononucleotide. *Nature Communications* **2016**, *7*, 13230.

(55) Hu, B.; Liu, T. L. Two electron utilization of methyl viologen anolyte in nonaqueous organic redox flow battery. *Journal of Energy Chemistry* **2018**, *27*, 1326–1332.

(56) Luo, J.; Wu, W.; Debruler, C.; Hu, B.; Hu, M.; Liu, T. L. A 1.51 V pH neutral redox flow battery towards scalable energy storage. *Journal of Materials Chemistry A* **2019**, *7*, 9130–9136.

(57) Liu, Y.; Goulet, M.-A.; Tong, L.; Liu, Y.; Ji, Y.; Wu, L.; Gordon, R. G.; Aziz, M. J.; Yang, Z.; Xu, T. A Long-Lifetime All-Organic Aqueous Flow Battery Utilizing TMAP-TEMPO Radical. *Chem* **2019**, *5*, 1861–1870.

(58) Korshunov, A.; Gibalova, A.; Grünebaum, M.; Ravoo, B. J.; Winter, M.; Cekic-Laskovic, I. Host-Guest Interactions Enhance the Performance of Viologen Electrolytes for Aqueous Organic Redox Flow Batteries. *Batteries & Supercaps* **2021**, *4*, 923–928.

(59) Korshunov, A.; Gibalova, A.; Gruenebaum, M.; Ravoo, B. J.; Winter, M.; Cekic-Laskovic, I. Supramolecular Viologen–Cyclodextrin Electrolytes for Aqueous Organic Redox Flow Batteries. *ACS Applied Energy Materials* **2021**, *4*, 12353–12364.

(60) Fan, H.; Wu, W.; Ravivarma, M.; Li, H.; Hu, B.; Lei, J.; Feng, Y.; Sun, X.; Song, J.; Liu, T. L. Mitigating Ring-Opening to Develop Stable TEMPO Catholytes for pH-Neutral All-Organic Redox Flow Batteries. *Advanced Functional Materials* **2022**, *32*, 2203032.

(61) Hu, M.; Wang, A. P.; Luo, J.; Wei, Q.; Liu, T. L. Cycling Performance and Mechanistic Insights of Ferricyanide Electrolytes in Alkaline Redox Flow Batteries. *Advanced Energy Materials* **2023**, *13*, 2203762.

(62) Hu, B.; Luo, J.; Hu, M.; Yuan, B.; Liu, T. L. A pH-Neutral, Metal-Free Aqueous Organic Redox Flow Battery Employing an Ammonium Anthraquinone Anolyte. *Angewandte Chemie International Edition* **2019**, *58*, 16629–16636.

(63) Luo, J.; Hu, M.; Wu, W.; Yuan, B.; Liu, T. L. Mechanistic insights of cycling stability of ferrocene catholytes in aqueous redox flow batteries. *Energy & Environmental Science* **2022**, *15*, 1315–1324.

(64) Luo, J.; Hu, B.; Hu, M.; Wu, W.; Liu, T. L. An Energy-Dense, Powerful, Robust Bipolar Zinc–Ferrocene Redox-Flow Battery. *Angewandte Chemie International Edition* **2022**, *61*, e202204030.

(65) Lv, X.-L.; Sullivan, P.; Fu, H.-C.; Hu, X.; Liu, H.; Jin, S.; Li, W.; Feng, D. Dextrosil-Viologen: A Robust and Sustainable Anolyte for Aqueous Organic Redox Flow Batteries. *ACS Energy Letters* **2022**, *7*, 2428–2434.

(66) Zhang, X.; Liu, X.; Zhang, H.; Wang, Z.; Zhang, Y.; Li, G.; Li, M.-j.; He, G. Robust Chalcogenophene Viologens as Anolytes for Long-Life Aqueous Organic Redox Flow Batteries with High Battery Voltage. *ACS Applied Materials & Interfaces* **2022**, *14*, 48727–48733.

(67) Wu, W.; Wang, A. P.; Luo, J.; Liu, T. L. A Highly Stable, Capacity Dense Carboxylate

Viologen Anolyte towards Long-Duration Energy Storage. *Angewandte Chemie International Edition* **2023**, *62*, e202216662.

(68) Yao, Y.; Ma, W.; Lei, J.; Wang, Z.; Lu, Y.-C.; Liu, L. Nonionic oligo(ethylene glycol)-substituted viologen negolytes for aqueous organic redox flow batteries. *Journal of Materials Chemistry A* **2023**,

(69) Song, W.; Peng, K.; Xu, W.; Liu, X.; Zhang, H.; Liang, X.; Ye, B.; Zhang, H.; Yang, Z.; Wu, L.; Ge, X.; Xu, T. Upscaled production of an ultramicroporous anion-exchange membrane enables long-term operation in electrochemical energy devices. *Nature Communications* **2023**, *14*, 2732.

(70) Feng, R.; Zhang, X.; Murugesan, V.; Hollas, A.; Chen, Y.; Shao, Y.; Walter, E.; Wellala, N. P. N.; Yan, L.; Rosso, K. M.; Wang, W. Reversible ketone hydrogenation and dehydrogenation for aqueous organic redox flow batteries. *Science* **2021**, *372*, 836–840.

(71) Peng, K.; Li, Y.; Tang, G.; Liu, Y.; Yang, Z.; Xu, T. Solvation regulation to mitigate the decomposition of 2,6-dihydroxyanthraquinone in aqueous organic redox flow batteries. *Energy & Environmental Science* **2023**, *16*, 430–437.

(72) Wellala, N. P. N.; Hollas, A.; Duanmu, K.; Murugesan, V.; Zhang, X.; Feng, R.; Shao, Y.; Wang, W. Decomposition pathways and mitigation strategies for highly-stable hydroxyphenazine flow battery anolytes. *Journal of Materials Chemistry A* **2021**, *9*, 21918–21928.

(73) Er, S.; Suh, C.; Marshak, M. P.; Aspuru-Guzik, A. Computational design of molecules for an all-quinone redox flow battery. *Chemical Science* **2015**, *6*, 885–893.

(74) Tong, L.; Goulet, M.-A.; Tabor, D. P.; Kerr, E. F.; De Porcellinis, D.; Fell, E. M.; Aspuru-Guzik, A.; Gordon, R. G.; Aziz, M. J. Molecular Engineering of an Alkaline Naphthoquinone Flow Battery. *ACS Energy Letters* **2019**, *4*, 1880–1887.

(75) Tabor, D. P.; Gómez-Bombarelli, R.; Tong, R. G., Liuchuan and Gordon; Aziz, M. J.; Aspuru-Guzik, A. Mapping the frontiers of quinone stability in aqueous media: implications for organic aqueous redox flow batteries. *Journal of Materials Chemistry A* **2019**, *7*, 12833–12841.

(76) Zhang, Q.; Khetan, A.; Er, S. A quantitative evaluation of computational methods to accelerate the study of alloxazine-derived electroactive compounds for energy storage. *Scientific Reports* **2021**, *11*, 4089.

(77) Sorkun, E.; Zhang, Q.; Khetan, A.; Sorkun, M. C.; Er, S. RedDB, a computational database of electroactive molecules for aqueous redox flow batteries. *Scientific Data* **2022**, *9*, 718.

(78) Gao, P.; Andersen, A.; Sepulveda, J.; Panapitiya, G. U.; Hollas, A.; Saldanha, E. G.; Murugesan, V.; Wang, W. SOMAS: a platform for data-driven material discovery in redox flow battery development. *Scientific Data* **2022**, *9*, 740.

(79) Li, T.; Zhang, C.; Li, X. Machine learning for flow batteries: opportunities and challenges. *Chemical Science* **2022**, *13*, 4740–4752.

(80) S. V., S. S.; Law, J. N.; Tripp, C. E.; Duplyakin, D.; Skordilis, E.; Biagioni, D.; Paton, R. S.; St. John, P. C. Multi-objective goal-directed optimization of de novo stable organic radicals for aqueous redox flow batteries. *Nature Machine Intelligence* **2022**, *4*, 720–730.

(81) Robb, B. H.; Farrell, J. M.; Marshak, M. P. Chelated Chromium Electrolyte Enabling High-Voltage Aqueous Flow Batteries. *Joule* **2019**, *3*, 2503–2512.

(82) Modak, S.; Kwabi, D. G. A Zero-Dimensional Model for Electrochemical Behavior and Capacity Retention in Organic Flow Cells. *Journal of The Electrochemical Society* **2021**, *168*, 080528.

(83) Guiheneuf, S.; Godet-Bar, T.; Fontmorin, J.-M.; Jourdin, C.; Floner, D.; Geneste, F. A new hydroxyanthraquinone derivative with a low and reversible capacity fading process as negolyte in alkaline aqueous redox flow batteries. *Journal of Power Sources* **2022**, *539*, 231600.

(84) Clegg, C. Characterizing Degradation in Organic Redox Flow Batteries. Ph.D. thesis, Dalhousie University, 2022.

(85) Jin, S.; Fell, E. M.; Vina-Lopez, L.; Jing, Y.; Michalak, P. W.; Gordon, R. G.; Aziz, M. J. Near Neutral pH Redox Flow Battery with Low Permeability and Long-Lifetime Phosphonated Viologen Active Species. *Advanced Energy Materials* **2020**, *10*, 2000100.

(86) Amini, K.; Pritzker, M. D. In situ polarization study of zinc–cerium redox flow batteries. *Journal of Power Sources* **2020**, *471*, 228463.

(87) Jin, S.; Jing, Y.; Kwabi, D. G.; Ji, Y.; Tong, L.; De Porcellinis, D.; Goulet, M.-A.; Pollack, D. A.; Gordon, R. G.; Aziz, M. J. A Water-Miscible Quinone Flow Battery with High Volumetric Capacity and Energy Density. *ACS Energy Letters* **2019**, *4*, 1342–1348.

(88) Li, X.; Gao, P.; Lai, Y.-Y.; Bazak, J. D.; Hollas, A.; Lin, H.-Y.; Murugesan, V.; Zhang, S.; Cheng, C.-F.; Tung, W.-Y.; Lai, Y.-T.; Feng, R.; Wang, J.; Wang, C.-L.; Wang, W.; Zhu, Y. Symmetry-breaking design of an organic iron complex catholyte for a long cyclability aqueous organic redox flow battery. *Nature Energy* **2021**, *6*, 873–881.

(89) Albertus, P.; Manser, J. S.; Litzelman, S. Long-Duration Electricity Storage Applications, Economics, and Technologies. *Joule* **2020**, *4*, 21–32.

(90) Reber, D.; Jarvis, S.; Marshak, M. The role of energy density for grid-scale batteries. *ChemRxiv* **2023**,